Ocean Engineering 88 (2014) 91–109

Contents lists available at ScienceDirect

Ocean Engineering

journal homepage: www.elsevier.com/locate/oceaneng

Numerical investigation of wave–structure interaction using OpenFOAM

L.F. Chen [a,*], J. Zang [a], A.J. Hillis [b], G.C.J. Morgan [c], A.R. Plummer [b]

[a] Department of Architecture and Civil Engineering, University of Bath, Bath BA2 7AY, UK
[b] Department of Mechanical Engineering, University of Bath, Bath BA2 7AY, UK
[c] Edenvale Young Associates Ltd., St Nicholas House, 31-34 High Street, Bristol BS1 2AW, UK

ARTICLE INFO

Article history:
Received 14 August 2013
Accepted 6 June 2014
Available online 11 July 2014

Keywords:
OpenFOAM
Nonlinear wave–structure interactions
Wave loading
Spectral decomposition

ABSTRACT

The present work is focused on the assessment of how OpenFOAM performs when applied to non-linear wave interactions with offshore structures for ranges of wave conditions. New modules have been further extended to advance the wave generation and wave absorbing capabilities of the code. The numerical results for wave interactions with a vertical surface piercing cylinder have been compared with physical experiments performed at Danish Hydraulic Institute (DHI). Comparisons between the numerical results and the measured data for three regular waves and four focused wave groups, have indicated that OpenFOAM is very capable of accurate modelling of nonlinear wave interaction with offshore structures, with up to 4th order harmonic correctly captured. Moreover, by using the crest-trough phase-based separation method, we can reproduce harmonic structure in the wave loading on the structure and free surface elevations.

1. Introduction

Wave–structure interaction is a key consideration for the safe and cost-effective design of coastal and offshore structures. Investigations using experiments and numerical simulations have been traditionally carried out to provide predictions for wave loading and wave run-up on the body, and wave scattering in the wave field. A worldwide interest in renewable energy was motivated by the oil crisis in 1973 (Folley et al., 2004). Recently, following the issues of climate change and energy demand, the development of marine renewable energy is attracting increasing attention. Wave energy devices and foundations supporting offshore wind turbines are subject to constant wave loads. These structures may be located in intermediate water depth, or in shallow water, where strongly nonlinear waves and breaking waves may cause damage to the structures. If marine renewable energy is to play a significant role in meeting the energy demand, all energy extraction devices and offshore wind turbine supporting structures must survive for many years without damage. Hence accurate design methods are required to estimate the hydrodynamic loads occurring in all wave conditions.

Physical experimentation is one of most common approaches for studying wave–structure interaction, with the advantages of reproduction of real hydrodynamics and easy implementation and repetition. The Morison equation and potential flow theory have also been widely used for the prediction of wave loading on offshore structures. Compared to physical experiments, they overcome the scale effect and are more economic. The Morison equation was proposed by Morison et al. (1950) and has been adopted as a standard method for slender offshore structures. As an empirical method, the Morison equation contains two empirical flow coefficients, the inertia and drag coefficients, which have to be determined from experimental measurements (Keulegan and Carpenter, 1958; Morison et al., 1950; Sarpkaya and Isaacson, 1981). The experiments could not be carried out for all wave conditions, meaning that in principle the Morison equation is not valid for all flow regimes. Additionally, according to Sarpkaya and Isaacson (1981), it only provides reasonable predictions when the structures are compact bodies, and the pressure distribution on these bodies is not provided completely. How to properly account for the nonlinear wave and breaking wave impact on the structures still remains a major challenge for using Morison equation.

In potential flow theory, the flow is assumed to be inviscid and irrotational. In numerical analysis, the computational domain is discretized into numerous cells or boundary elements and then

---

[*] Corresponding author. Tel.: +44 7774443761.
E-mail addresses: chenlifen239@gmail.com, lc499@bath.ac.uk (L.F. Chen), j.zang@bath.ac.uk (J. Zang), A.J.Hillis@bath.ac.uk (A.J. Hillis), gerald@edenvaleyoung.com (G.C.J. Morgan), a.r.plummer@bath.ac.uk (A.R. Plummer).

http://dx.doi.org/10.1016/j.oceaneng.2014.06.003
0029-8018/

the velocity potentials are calculated for each element. Such techniques are widely used in linear and weakly non-linear wave–structure interaction problems due to low computational cost and mature numerical techniques. Second order wave diffraction from structures has been successfully applied to the studies of wave interactions with fixed and floating bodies by Chau and Eatock Taylor (1992), Kim and Yue (1989, 1990), Stansberg and Kristiansen (2005), Walker et al. (2007, 2008), Zang et al. (2006, 2009), etc. But the limitation for using second order wave theory is that the hydrodynamic forces and free surface elevations beyond the second order cannot be included. For including the high order harmonics, numerical studies based on fully non-linear potential flow theory have been developed and applied to both coastal and offshore problems (Bai and Eatock Taylor, 2007; Grilli et al., 2001a, 2001b; Ma et al., 2001a, 2001b). It is a great challenge for potential flow theory to capture the nonlinear free surface correctly when wave breaking occurs, which limits its application to strongly nonlinear wave cases.

For highly non-linear wave–structure interaction, including breaking wave impact and the evolution of vortices, Computational Fluid Dynamics (CFD) based on Navier–Stokes equations is used. With the rapid development of high performance computing technology, the use of CFD tools is becoming increasing important in engineering design work. OpenFOAM, a free, open-source c++ library for continuum-mechanics problems, has been applied to a selection of common problems in coastal and offshore engineering. Its capability in coastal engineering was confirmed by Morgan et al. (2010, 2011). The experimental results for the propagation of regular waves over a submerged bar have been reproduced in his numerical simulations, with up to 8th order harmonics correctly modeled. Jacobsen et al. (2012) have extended the OpenFOAM with a generic wave generation and absorption method to model wave propagation and wave breaking. Higuera et al. (2013a, 2013b) have implemented specific boundary conditions for realistic wave generation and active absorption. A robust three dimensional, two-phase numerical model for practical applications in coastal engineering is presented.

The present work is focused on the assessment of how OpenFOAM performs when applied to non-linear wave interactions with offshore structures for ranges of wave conditions. In this paper, the numerical results for wave interactions with a vertical surface piercing cylinder, a typical offshore wind turbine foundation and basic part of many offshore structures are presented and compared with physical experiments performed at Danish Hydraulic Institute (DHI). The existing solver, interFoam, supplied with OpenFOAM has been selected for the two-phase flow modeling based on the unsteady, incompressible Navier–Stokes equations. New modules have been further extended to advance the wave generation and wave absorbing capabilities of the code first developed by Morgan et al. (2010). A series of experiments performed in DHI's shallow basin in 2009 by Zang et al. (2010) have been reproduced using OpenFOAM to examine its accuracy and performance for predicting nonlinear wave–structure interaction problems. The decomposition of the measured signals into its fundamental harmonics has also been carried out to examine the importance of high order wave loading on the structure.

2. Numerical methods

2.1. Governing equations

Navier–Stokes equations are generally used to describe the motion of fluid continuum. In terms of an incompressible fluid, the Navier–Stokes equations can be written as a mass conservation equation and a momentum conservation equation, which are listed as follows,

$$\nabla \times \overrightarrow{U} = 0 \tag{1}$$

$$\frac{\partial \rho \overrightarrow{U}}{\partial t} + \nabla \times (\rho \overrightarrow{U}\,\overrightarrow{U}) - \nabla \times (\mu \nabla \overrightarrow{U}) - \rho \overrightarrow{g} = -\nabla p - \overrightarrow{f}_{\sigma} \tag{2}$$

where, ρ is the fluid density, p is the fluid pressure and μ is the dynamic viscosity. $\overrightarrow{U}$ and $\overrightarrow{f}_{\sigma}$ are the fluid velocity and the surface tension, respectively. There are four unknown variables in Navier–Stokes equations, the fluid pressure and each component of the fluid velocity, when considered in three dimensions.

2.2. Solver and algorithm

The default solver, supplied with OpenFOAM, for simulating the motions of the interface between two phases is *interFoam*. It is designed for unsteady, incompressible Navier–Stokes equations based on the merged PISO-SIMPLE (PIMPLE) algorithm to solve the pressure–velocity coupling. The Semi-Implicit Method for Pressure-Linked equations (SIMPLE) algorithm allows the calculation of pressure on a mesh from velocity components by coupling the Navier–Stokes equations with an iterative procedure. The Pressure Implicit Splitting Operator (PISO) algorithm has been applied in the PIMPLE algorithm to rectify the pressure–velocity correction. A detailed description of the SIMPLE and PISO algorithm can be found in Ferziger and Peric (1999) and Issa (1985), respectively.

Generally speaking, the Navier–Stokes equations are first integrated over the whole solution domain and time domain. Second, the solution and time domain are discretized into a number of cells and time steps, respectively. Dependent variables and other properties then can be denoted by the values at the centroids. In OpenFOAM the spatial discretization is based on arbitrarily unstructured meshes which consist of arbitrary convex polyhedral cells. These cells should be continuous, which means they do not overlap with each other and fill the whole computational domain. The main control over time step is the Courant number, which represents the portion of a cell that the flow will transverse due to advection effect in one time step. The Courant number has the following form for the one dimensional case (Courant et al., 1967),

$$Co = \frac{\delta t |U|}{\delta x} \tag{3}$$

where, δt is the maximum time step, δx is the cell size in the direction of the velocity and $|U|$ is the magnitude of the velocity at that location. To ensure stability of the model and improve accuracy, the maximum value of the Courant number should be 1 throughout the whole domain (Courant et al., 1967).

Based on the computational mesh, the Navier–Stokes equations are subsequently discretized into a set of algebraic equations, which are pressure and velocity equations in the PIMPLE algorithm (The OpenFOAM® Foundation, 2011a, 2011b). The PIMPLE algorithm is composed of an implicit momentum predictor and several pressure–velocity correctors. In the PIMPLE loop, the velocity equations are firstly solved by using the velocity and pressure fields of the previous time step, known as momentum predictor. The velocity and pressure are corrected several times afterwards to satisfy mass conservation. Several methods are offered by OpenFOAM to solve the set of linear equations, such as the geometric–algebraic multi-grid (GAMG) and faster diagonal incomplete-cholesky (FDIC) methods (Datta, 2010).

Additionally, there are several built-in numerical schemes in OpenFOAM to discretize terms that may be found in a PDE, such as derivative terms. The Standard Gaussian finite volume integration method, which based on summing values on cell faces, is usually used to get higher accuracy of the integrations for derivative terms

(LeVeque, 2002). The values on cell faces are interpolated from cell centres. There are several interpolation schemes, such as central differencing, upwind differencing and blended differencing methods, are provided for users to choose on a case-by-case basis.

2.3. Free surface tracking

The volume of fluid (VOF) method has been applied in OpenFOAM for locating and tracking the free surface. The VOF method was presented by Hirt and Nichols (1981) and is based on the Marker and Cell (MAC) method. In the VOF method, each of the two phases is considered to have a separately defined volume fraction. When the cell is empty of water but filled with air, the value of volume fraction function is 0; when the cell is full of water, it is 1; and when the interface cuts the cell, this function is between 0 and 1. That is,

$$\alpha(x,t)=\begin{cases}1, & \text{water}\\ 0, & \text{air}\\ 0<\alpha_s<1, & \text{freesurface}\end{cases} \tag{4}$$

The two-phase flow is considered as a mixed fluid, and the density and dynamic viscosity can then be presented as:

$$\rho=\alpha\rho_1+(1-\alpha)\rho_2$$
$$\mu=\alpha\mu_1+(1-\alpha)\mu_2 \tag{5}$$

The volume fraction function can be determined by solving an advection equation:

$$\frac{\partial\alpha}{\partial t}+\nabla\times(\alpha\vec{U})+\nabla\times(\alpha(1-\alpha)\vec{U}_\alpha)=0 \tag{6}$$

where the last term on the left-hand side is an artificial compression term to limit numerical diffusion and $\vec{U}_\alpha$ is a relative compression velocity (Weller et al., 1998).

2.4. New boundary treatments

A CFD modelling process should have the ability to represent various physical boundary conditions accurately. To achieve this, OpenFOAM imposes constraints on the available variables such as pressure, velocity and volume fraction in two-phase flow cases. But conditions for water waves and far field are not supplied with OpenFOAM by default. In order to apply OpenFOAM to wave hydrodynamics, additional functions have been further extended to advance the wave generation and absorbing capacities of the numerical model which was first developed by Morgan et al. (2010), and will be described below.

2.4.1. Wave generation

A new boundary condition was added to OpenFOAM to allow the generation of regular waves, random waves and focused wave groups as input waves. According to Morgan et al. (2010), a direct simulation of a piston-type wave-maker is slow, so in this study, the wave generation is via the flux into the computational domain through a vertical wall. The volume fraction and horizontal and vertical velocities at the wave inlet boundary faces are specified.

A simple limiting function is used to convert the water surface elevation into a volume fraction:

$$\alpha(x,z,t)=\left(\max\left[\min\left([\eta(x,z,t)-z],\frac{\Delta z}{2}\right),-\frac{\Delta z}{2}\right]+\frac{\Delta z}{2}\right)/\Delta z \tag{7}$$

where Δz is a small parameter specifying the width of the free surface zone and for regular waves, $\eta(x,t)=A\cos(kx-\omega t)$.

The velocities on the inlet boundary are then generated by multiplying the velocities from the selected wave theory by this volume function so that the velocities in the air are zero and the velocities in the water are as calculated. The velocities of regular waves are based on linear Stokes' wave theory,

$$u(x,z,t)=\frac{gkA}{\omega}\frac{\cosh k(z+h)}{\cosh kh}\sin\varphi \tag{8}$$

$$w(x,z,t)=\frac{gkA}{\omega}\frac{\sinh k(z+h)}{\cos kh}\cos\varphi \tag{9}$$

in which, $\varphi=kx-\omega t$ and k is the wave number, h is the water depth.

In this study, apart from regular wave test cases, we also report on the interaction of focused wave groups with a surface-piecing vertical cylinder, which was studied experimentally by Zang et al. (2010a, 2010b). The focused wave group overcomes the shortcomings of regular waves which lack representation of the broadband spectrum of real ocean waves. Additionally, compared to traditional random waves, the frequency spectrum and phase of the components can be controlled in the focused wave group, which enables the realistic modelling of an extreme event within a short time. This makes both physical experiments and numerical simulation very efficient. There are another two advantages in using the focused wave group: first to provide a model for transient events, and second to allow the separation of the focused wave group into its fundamental components (Zang et al., 2006).

The free surface elevation for a focused wave group is defined by:

$$\eta(t)=\sum_{n=1}^{N}a_n\cos(\varphi_n) \tag{10}$$

in which

$$a_n=A\frac{S(\omega_n)\times\Delta\omega}{\sum_{n=1}^{N}S(\omega_n)\times\Delta\omega} \tag{11}$$

$$\varphi_n=k_n(x-x_0)-\omega_n(t-t_0)+\varepsilon_n \tag{12}$$

where A is the crest value of the focused wave group, x_0 and t_0 are the focus distance and time, respectively. $\Delta\omega$ is the increment of the angular frequency, ε_n is the random initial phase and k_n is the wave number of the nth wave. $S(\omega_n)$ is the wave energy spectrum which provides information on the wave energy distribution with wave frequency ω_n. There are various forms of wave spectrum, including Neumann, Pierson–Moscowitz and JONSWAP. JONSWAP is the most widely used spectrum for coastal and offshore problems due to its excellent agreement with measured results. A JONSWAP spectrum is selected in numerical simulations reported in this paper as well as in experimental tests described in Zang et al. (2010a, 2010b). The expression of the JONSWAP spectrum is Hasselmann et al. (1973):

$$S(\omega)=\alpha g^2\frac{1}{\omega^5}\exp\left[-\frac{5}{4}\left(\frac{\omega_m}{\omega}\right)^4\right]\gamma^a \tag{13}$$

in which

$$a=\exp\left[-\frac{(\omega-\omega_m)^2}{2\sigma^2\omega_m^2}\right] \tag{14}$$

$$\sigma=\begin{cases}0.07, & \omega\le\omega_m\\ 0.09, & \omega>\omega_m\end{cases} \tag{15}$$

and α is chosen as 0.0081 empirically, ω_m is the peak circular frequency of the focused wave group, g is the acceleration due to gravity. The peak of the spectrum is defined by γ. The peak wave amplitude increases with the γ. The value of 3.3 was used here as it shows a good representation for severe storms in the North Sea (Taylor and Williams, 2004). The velocities of focused wave groups are calculated by summing the velocities of regular waves presented in Eqs. (8) and (9).

Several boundary conditions for wave generation are currently available in literature, such as Jacobsen et al. (2012) and Higuera et al. (2013a, 2013b). For the model presented in this paper, the volume fraction is determined based on the location of the face center relative to wave elevation η and calculated by Eq. (7), whereas the volume fraction of the model presented by Jacobsen et al. (2012) is specified as A_w/A_f, where A_w is the area of the wet sides of the boundary face and A_f is the area of the boundary face. The time series of wave elevation at $x=1.0$ m from the model presented by Jacobsen et al. (2012) and the model presented in this paper are shown in Fig. 1. The water depth is 0.505 m, wave height is 0.12 m and wave length is 3.16 m. The grid cells have a resolution of mainly 0.045 m in the horizontal direction and 0.01 m in the vertical direction. It can be seen from the graph that both models can generate specific waves as desired with same mesh resolution without large discrepancy.

Higuera et al. (2013a, 2013b) introduces a specific module to replicate laboratory wavemaker velocity profiles. A time series of the wavemaker displacement or velocity is given at the input boundary and, if the free surface is not provided, the corresponding constant velocity profile along the whole water column is applied and multiplied with the volume fraction in each cell in order not to introduce air velocity.

2.4.2. Far field boundary conditions

In this study, the damping zone method has been applied to represent far field boundary conditions, aiming to avoid reflection at the downstream of the flume (Celebi et al., 1998). In this method, an artificial damping term $\rho\theta\vec{U}$ is added to the momentum equation, and

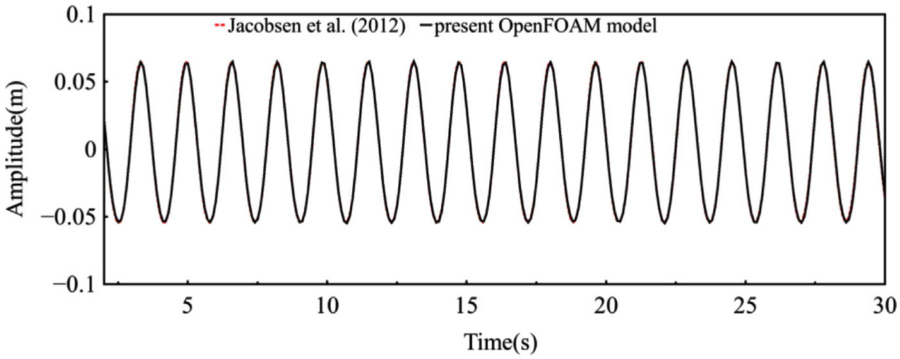

Fig. 1. Time histories of wave elevation at $x=0.1$ m generated from both two models.

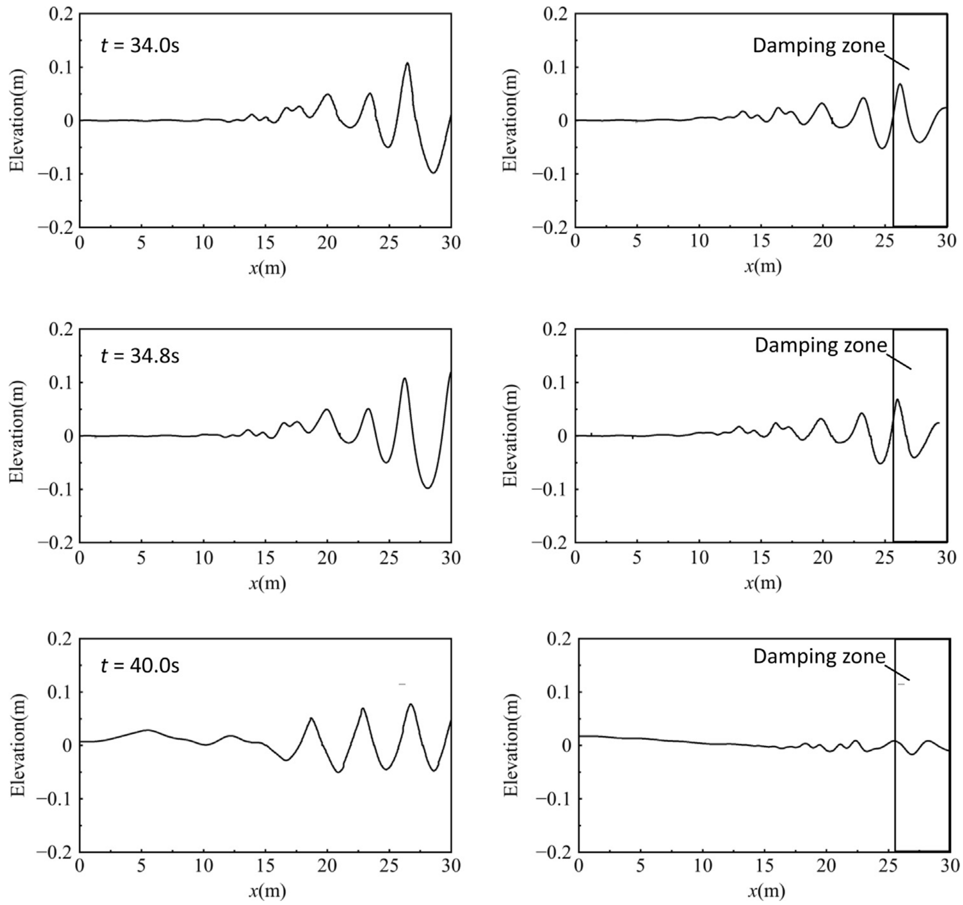

Fig. 2. Wave profiles along the central line of the tank at several time intervals.

then Eq. (2) can be rewritten as,

$$\frac{\partial \rho \vec{U}}{\partial t} + \nabla \times (\rho \vec{U}\vec{U}) - \nabla \times (\mu \nabla \vec{U}) + \rho \theta \vec{U} = \rho \vec{g} - \nabla p - \vec{f}_{\sigma} \qquad (16)$$

in which

$$\theta = \begin{cases} \dfrac{x - x_0}{x_1 - x_0}\theta_1, & x_0 < x < x_1 \\ 0, & 0 < x < x_0 \end{cases} \qquad (17)$$

where x are coordinates from paddle, x_0 is the start point of the damping zone and $(x_1 - x_0)$ is the length of the wave tank. Additionally, θ_1 is damping coefficient which can be determined empirically (Larsen and Dancy, 1983; Romate, 1992).

A numerical sponger layer is applied in the model presented by Jacobsen et al. (2012) to avoid reflection of waves from outlet boundaries. In this method, the volume fraction and the fluid velocity at every time step are relaxed towards prescribed values, α_{target} and $U_{target,}$ based on a relaxation function. The relaxation function decreases from 1 at the beginning of the damping zone, to 0 at the end of the zone. For Higuera et al. (2013a), an active wave absorption method is applied to dissipate the outgoing waves. The correction velocity profile from the existing theories of active wave absorption systems, such as the 2D active absorption method, Quasi-3D and 3D absorption methods, is specified at the outlet boundary.

Fig. 2 shows the wave profiles of focused wave groups along the central line of the tank at several time instants to show the effectiveness of the adopted relaxation technique. The total length of the tank is 30 m with 4.75 m long relaxation zone, which is about 1.5 times of peak wave length and damping coefficient θ_1 is set to be 2.0. Without a relaxation zone, a standing wave is produced at the downstream boundary due to the wave reflection. With the damping technique, the results have shown that wave energy dissipates gradually in the damping zone without causing much wave reflection to the wave field. With this technique, shorter wave flume will be needed without generated significant reflection from the open boundary. Hence, computational time can be reduced.

The parameter study on regular waves was carried out to assess the effect of the damping coefficient θ_1 and length of the damping zone on the absorption performance of the method. Two separate comparisons were made. In the first comparison, the damping coefficient is set to be 0.5, 2, 3 and 10 with a 2L long damping zone. And in the second comparison, the length of the damping zone varies from 1L to 5L with the damping coefficient set to be 2. Here, L is the wave length. The wave profiles of regular waves along the central line of the wave tank at the time of 24 times of the wave period are shown in Fig. 3. Note that the length of the tank is increased to 35 m in order to have a longer wave damping zone. It can be seen that without the damping zone a standing wave is produced, and with the damping technique wave energy is dissipated gradually in the relaxation zone. This phenomenon was observed in Fig. 2 for focused wave groups as well. The reflection coefficient, the ratio between the incident wave amplitude of the first harmonic and the amplitude of the reflected wave, is plotted as a function of the wave damping coefficient and the length of the damping zone as shown in Fig. 4 (Goda and Suzuki, 1976). From Fig. 4(a), the reflection coefficient is about 11% when the damping coefficient is 0.5 and it decreases with the increase of the damping coefficient to its lowest point and then increases with the increase of the damping coefficient. This trend is consistent with Romate (1992) who stated that there is little dissipation for small values of the damping coefficient and the damping zone itself will act as a boundary with large value of damping coefficient. The value of 2 results in about 1% reflection when using a damping zone that is two wave lengths long. It can be seen from Fig. 4(b) that the reflection coefficient decreases with the increase of the length of the damping zone. It is less than 2% even with a damping zone that is one wave length long.

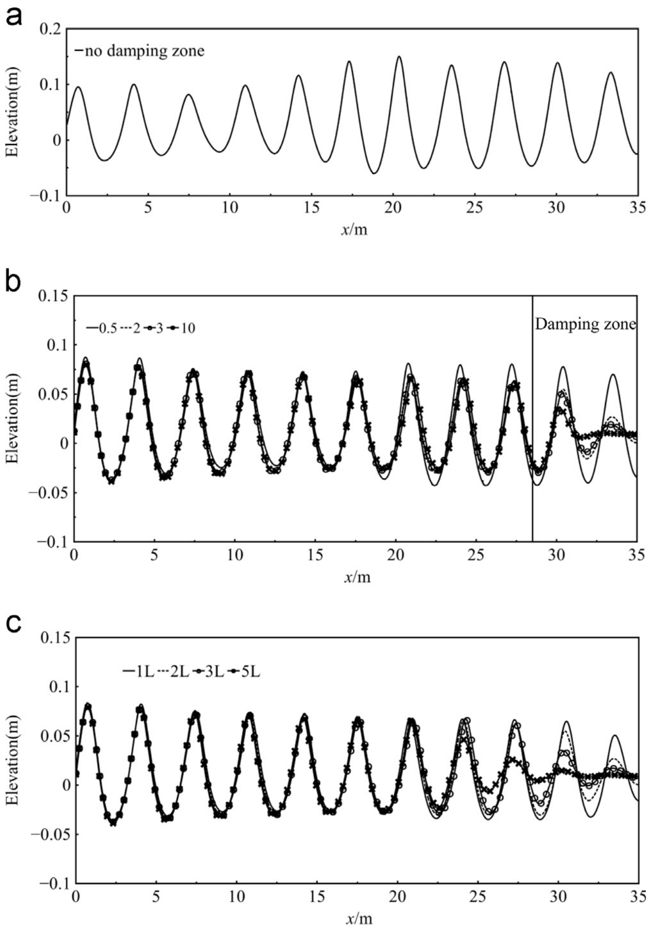

Fig. 3. Wave profile along the central line of wave tank at the time of 24T, where T is the wave period. (a) Without the damping zone, (b) with various damping coefficients (the length of the damping zone is kept the same, as 2L, in which L is the wave length and (c) with various lengths of damping zone (the damping coefficient is kept same, as 2).

According to Mendez et al. (2001), the existence of sponge layers would lead to an increase in the mean water level. In the simulations presented in this paper, there are no significant free surface changes over 20 wave periods, as shown in Fig. 1. This means that the current calculations do not suffer from this effect. But further analysis will be carried out to investigate the possible effect on the mean water levels.

3. Validation and discussions

3.1. Experimental setup

The experiments performed at DHI, Denmark for regular waves and focused wave groups hitting a surface-piercing vertical cylinder have been reproduced numerically using OpenFOAM in this study and some of the details of the experiments are given in Zang et al. (2010a, 2010b). The DHI shallow water basin (35 m × 25 m) was used for the tests with a water depth of 0.505 m. The wave field is created by a segmented piston paddle array installed at one end of the water basin. A cylinder of diameter 0.25 m was suspended from a rigid frame, leaving only a 1 mm gap beneath to the bed of the basin. The cylinder was located at 7.52 m from the paddles in the centre of the tank. The total horizontal hydrodynamic force on the cylinder was measured via

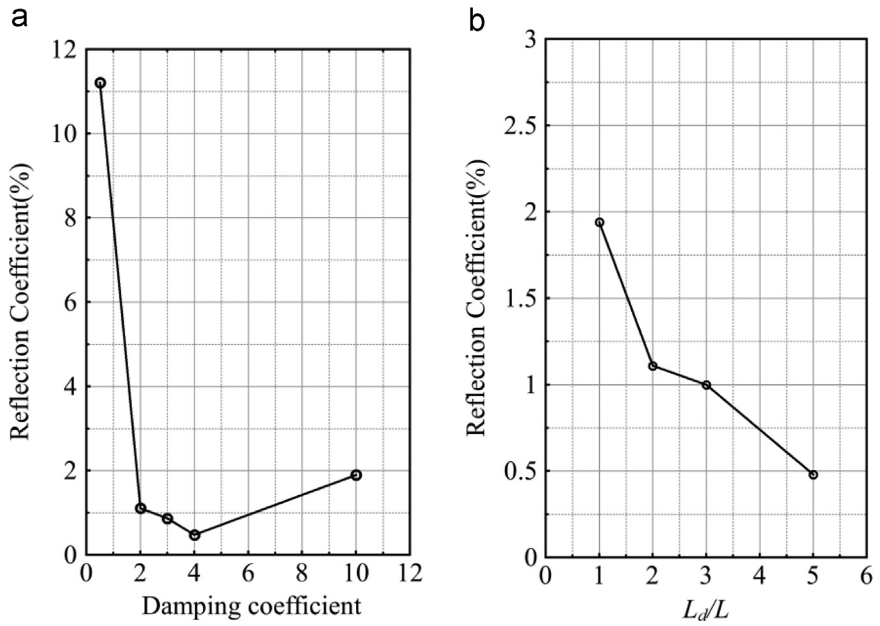

Fig. 4. Reflection coefficients (a) plotted as a function of the damping coefficient, (b) plotted as a function of L_d/L, in which L_d is the length of the damping zone and L is the wave length.

4 load cells on the top of the cylinder, and 19 wave gauges were placed to monitor the wave field around the cylinder. The layout for the wave gauges can be seen in Fig. 5. The results shown in this paper correspond to wave gauges 1, 5, 9, 13, 17 and 19.

All the test cases shown in this paper were carried out for regular waves and focused wave groups with varying wave steepness and wave frequencies similar to the experiments. Tests for focused wave groups and the same wave groups inverted were carried out in pairs. Each tall crest in the crest focussed wave group is replaced by a deep trough in the inverted form, referred to as a trough focussed wave group. Numerical results for three regular waves and four different crest focused wave groups are discussed in this paper, referred to as cases R1, R2, R3 and cases F1, F2, F3 and F4. Cases R1/F1 and R2/F2 correspond to the same slenderness ($ka=0.37$) and same depth ($kh=1.39$) for the cylinder, but have different steepness ($kA_1=0.1$, and $kA_2=0.2$). Similarly, cases F3 and F4, whose wave length is longer compared to the cases F1 and F2, have same slenderness and depth, but different steepness. Here k is wave number, a is cylinder radius, A is the crest value of focused wave group, h refers to water depth. The wave parameters are shown in Table 1.

3.2. Computational domain

In order to reproduce the experiments, a 3D numerical tank is setup. According to Zang et al. (2010a, 2010b), even the largest wave in their experimental tests appears to have a small drag force if not completely negligible. The dominant term in the wave loading on the cylinder is the inertia force. Due to the lateral symmetry of the problem, the numerical domain is truncated in the symmetry plane, with a typical layout illustrated in Fig. 6. The total length of the computational domain is 15 m with a relaxation zone of 1.5L. L is the wave length. The damping coefficient is set to be 2. The width of the solution domain is 2 m corresponding to 16a, where a is the cylinder radius. The water depth is 0.505 m. Additionally, there is a distance equivalent to the water depth (0.505 m) above the still water level to allow for motion of the air above the free surface as a result of wave action. The laminar flow model of OpenFOAM-2.1.0 is used in all computations in this paper. Most cases in this paper were computed using a single computer of an Intel “Core i7-2006”—based quad-core processors and 16 GB of RAM. The cases shown in Table 2 were computed with 8 cores using an Aquila HPC system at the University of Bath.

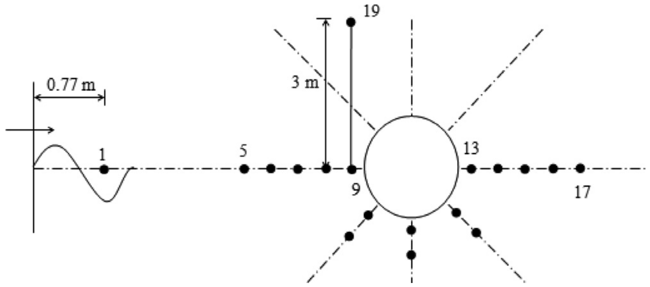

Fig. 5. The layout of wave gauges in the experiments.

Table 1
Wave parameters used in this study.

case ID	R1/F1	R2/F2	R3/F3	F4
T (s)	1.22	1.22	1.63	1.63
F (Hz)	0.82	0.82	0.61	0.61
A (m)	0.035	0.07	0.06	0.12
ka	0.37	0.37	0.25	0.25
kA	0.1	0.2	0.1	0.2
kh	1.39	1.39	0.86	0.86

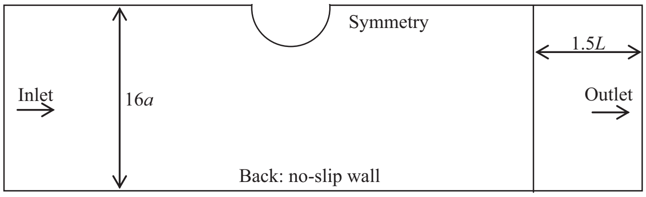

Fig. 6. Computational Domain. a is cylinder radius and L is wave length.

The overall numerical solution of hydrodynamic problems is broadly affected by the mesh used. Certain criteria should be satisfied to generate a high quality mesh to ensure a valid, and hence accurate, solution. *blockMesh*, a built-in mesh generation utility supplied with OpenFOAM, is used in this paper for generating meshes of blocks of hexahedral cells. The mesh consists of a multi-level grid: In areas without structural influence, including the walls where a no-slip condition is applied, the grid cells have a resolution of mainly Δx in the horizontal direction and Δz in the vertical direction, which are shown in Table 2. A finer mesh is used in areas around the cylinder. The diameter of the refinement area is about $5D$, where D is the diameter of the cylinder. Vertical cell sizes are graded so that the cells at the bed and at the top of the computational domain are four times bigger than those at the free surface. An over view of the mesh can be seen in Fig. 7.

The sensitivity of the model to the refinement and density of the mesh was assessed by using four different meshes. These meshes were labelled as 0, 1, 2 and 3 and their basic parameters can be found in Table 2. The maximum Courant number is set to be 0.5. The initial time step was set to be 0.01 s and is modified automatically according to the Courant number (see Eq. (3)). The time histories of wave run-up at the front stagnation point of the cylinder (WG9) using four different meshes are shown in Fig. 8. It can be seen that the model is convergent using the resolution of mainly $L/70$ in the horizontal direction and $H/8$ in the vertical direction with a refinement factor of 2.

The total cell numbers, the simulated time, the number of cores in which the case has been running and the corresponding total run time can be found in Table 2as well.

Table 2
Mesh parameters and computational cost.

Mesh scheme	$\Delta x=\Delta y$	Δz	Refinement factor	Cell number (million)	Cores	Simulated/ run time (h)
0	$L/240$	$H/8$	2	15.71212	4	$24.5T/157.45$
1	$L/70$	$H/8$	2	8.333943	8	$24.5T/126.20$
					4	$24.5T/85.00$
2	$L/35$	$H/8$	2	2.038868	8	$24.5T/11.34$
3	$L/70$	$H/12$	2	12.480719	8	$24.5T/207.6$

[*] L is the wave length, H is the wave height and T is wave period.

*Refinement factor is the ratio between the grid resolution of the areas without structural influence and refinement areas.

3.3. Boundary and initial conditions

The general specification of each physical boundary condition in this study is described in the following section.

3.3.1. Solid wall conditions

Soil or bed conditions and solid, impermeable structures can be specified as solid wall conditions. The *free-slip* and *no-slip* condition can be assigned to field variables to represent this kind of boundary condition. The *free-slip* condition means that the normal component is zero while the tangential component is unaffected. While for *no-slip* condition, all three components are constrained to a value of zero. In this study, the *no-slip* condition for velocity has been used in all cases for solid wall conditions. The boundary conditions used for pressure and volume fraction are specified with zero gradient for solid wall conditions. The back wall and the bed of the tank, shown in Fig. 6, are in this category.

3.3.2. Atmospheric conditions

This kind of boundary has the velocity set to *pressureInletOutletVelocity*, a default boundary condition supplied with OpenFOAM. This boundary condition applies zero-gradient on all components of the velocity except where there is inflow, in which case a fixed-value condition is applied. The water volume fraction is set to zero. The *totalPressure* condition is set for pressures. When the velocities change, the pressures are adjusted accordingly. This condition was assigned to the top of the tank in this study.

3.3.3. Symmetry plane

Only half of the domain is modelled in a problem whose solution domain and boundary conditions are symmetric about a plane to reduce computational time. In this case, one side of domain and the surface of the cylinder are set using *symmetryPlane*, which means the component of the gradient normal to the plane is zero.

3.3.4. Wave conditions

As stated in Section 2.4.1, new boundary conditions have been developed to generate specified waves, including both regular waves and random waves. In the present research, the new developed modules for generating regular waves and focused wave groups are named as *multiphaseWaveVelocity* and *multiphaseJONSWAPWaveVelocity*. They were applied to the inlet of the numerical wave tank with waves traveling from left to right. The wave amplitude A, wave length L, and water depth h are required

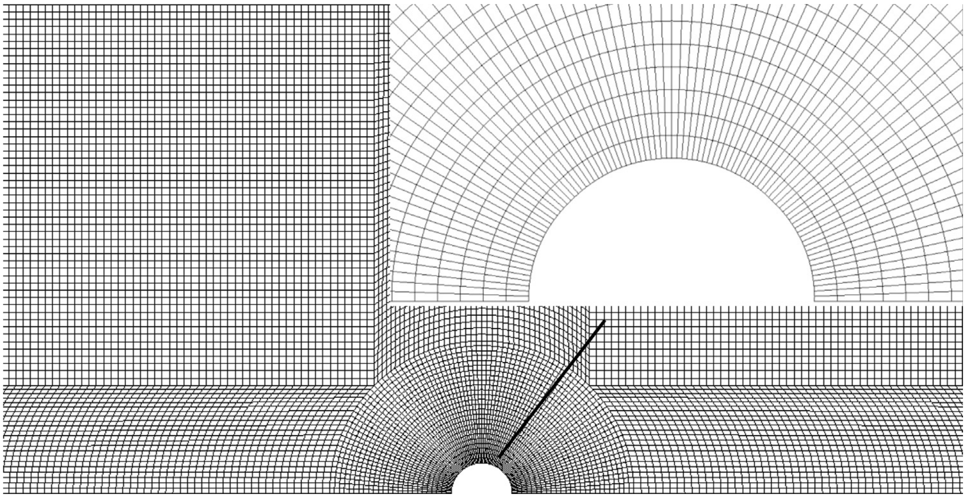

Fig. 7. Multi-block grid system employed.

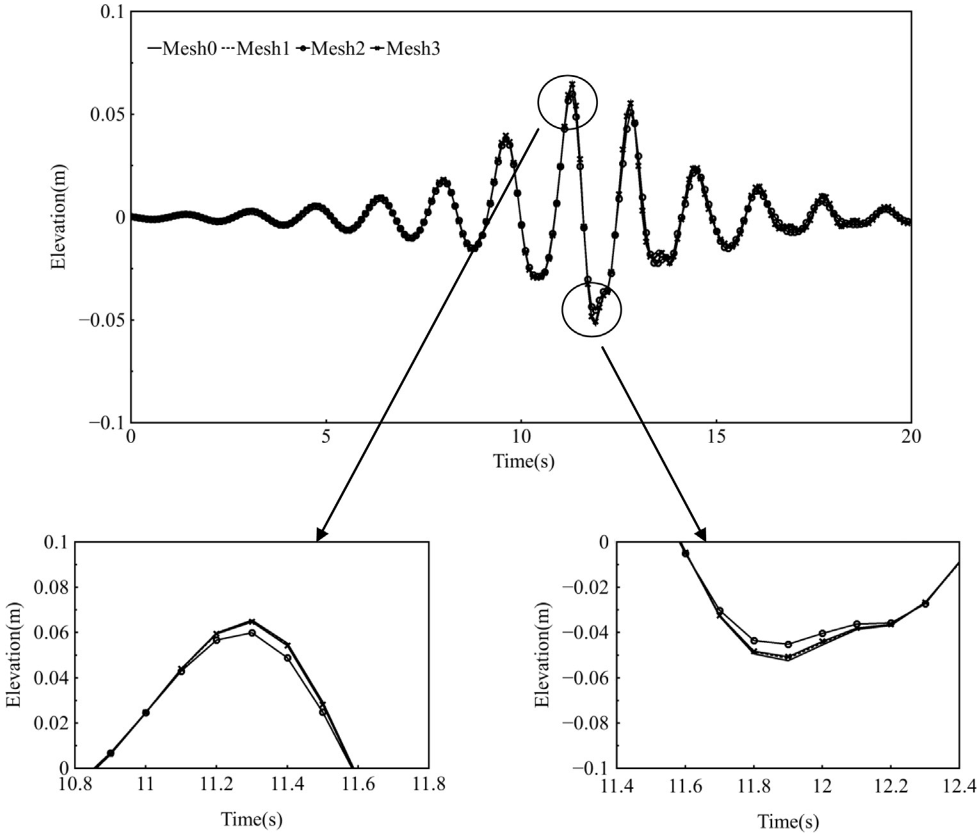

Fig. 8. Time histories of free surface elevation at WG9 obtained using four mesh schemes.

to be specified in the new module for generating regular waves. Likewise, the wave crest A, peak frequency f, water depth h, focus distance x_0 and focus time t_0 are used to determine the wave profile of focused wave groups.

3.3.5. *Far field boundary condition*

This new boundary condition has been described in Section 2.4.2 in this paper, and was applied at the outlet of the numerical wave tank to avoid any reflections. The start point of the relaxation zone and damping coefficient must be given by users. In this study, a size 1.5L damping zone has been used and the damping coefficient was set to 2.0.

3.4. *Comparisons with experimental data*

3.4.1. *Regular waves*

3.4.1.1. Free surface elevations. Both numerical and experimental results for the time histories of the free surface elevations at WG1 and WG9 for case R2 are shown in Fig. 9, as well as the corresponding amplitude spectra obtained by applying the FFT algorithm to the time histories shown on the left hand side of Fig. 9. The wave steepness and wave length of case R2 are 0.2 and 2.11 m, respectively. As the wave generation in the numerical simulation is via the flux into the computational domain through a fixed vertical wall, which is different from wave generation by piston paddles in the experiments, a careful match between experiments and numerical models for the first wave gauge (WG1, 0.77 m from the paddle) was made to ensure the incoming waves in the numerical tank are close to the waves generated in the experiments. From the results for WG9, which is 2 mm in front of the upstream stagnation point of the cylinder and 7.5 m from the wave paddles, it can be seen that the present numerical model can represent the frequency of all major harmonics which are present, and predict the amplitude of these harmonics to a reasonable degree of accuracy.

The time series of free surface elevation at WG9 and the corresponding amplitude spectra for cases R1 and R3 are presented in Fig. 10. Comparisons among cases R1, R2 and R3 reveal that steeper waves (R2) or longer waves (R3) show stronger nonlinearity with steeper and distorted wave shapes. Additionally, in the amplitude spectra diagrams, the cases R2 and R3 have higher 2nd order harmonics and some 3rd and even 4th order harmonics can be clearly seen in both numerical and experimental results. For case R1, the contributions of higher order free surface elevation above 1st order is only about 20% of its linear component, compared to about 30% and 40% for cases R2 and R3, respectively. Comparing the cases R1 and R2, the linear wave run-up at the stagnation point are 0.039 m and 0.095 m respectively, which are about 11% and 36% larger than its incoming wave amplitude, while the 2nd order terms of the wave run-up are 0.003 m and 0.03 m, which are about 8.6% and 42.9% of its incoming wave amplitude, respectively. It is clear that the high order harmonics can be predicted with a reasonable accuracy by the numerical simulation using OpenFOAM.

3.4.1.2. Horizontal wave loading. The time series of horizontal wave loading on the cylinder and corresponding amplitude spectra for all three regular wave cases are presented in Fig. 11. As with the free surface elevations, the agreements between the predicted and the measured horizontal forces are generally good, with similar values and profiles. It can be seen from the figures that steeper waves lead to stronger non-linear wave–structure interactions and more significant nonlinear effect. For reference, the contributions of higher order horizontal forces on the cylinder above 1st order

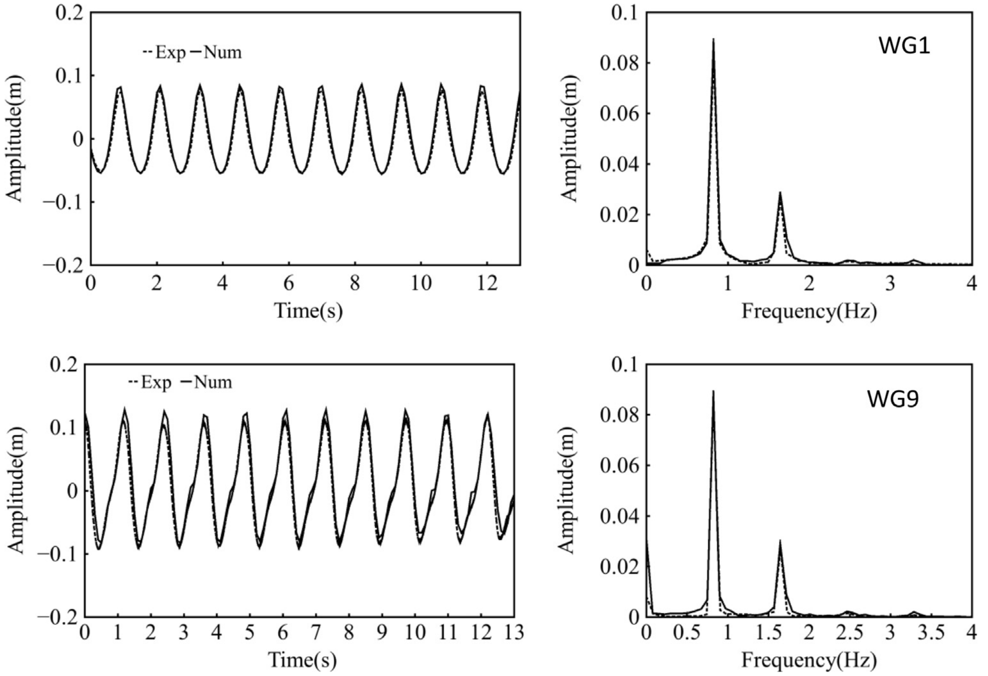

Fig. 9. Time series of free surface elevation and amplitude spectra for regular wave case R2.

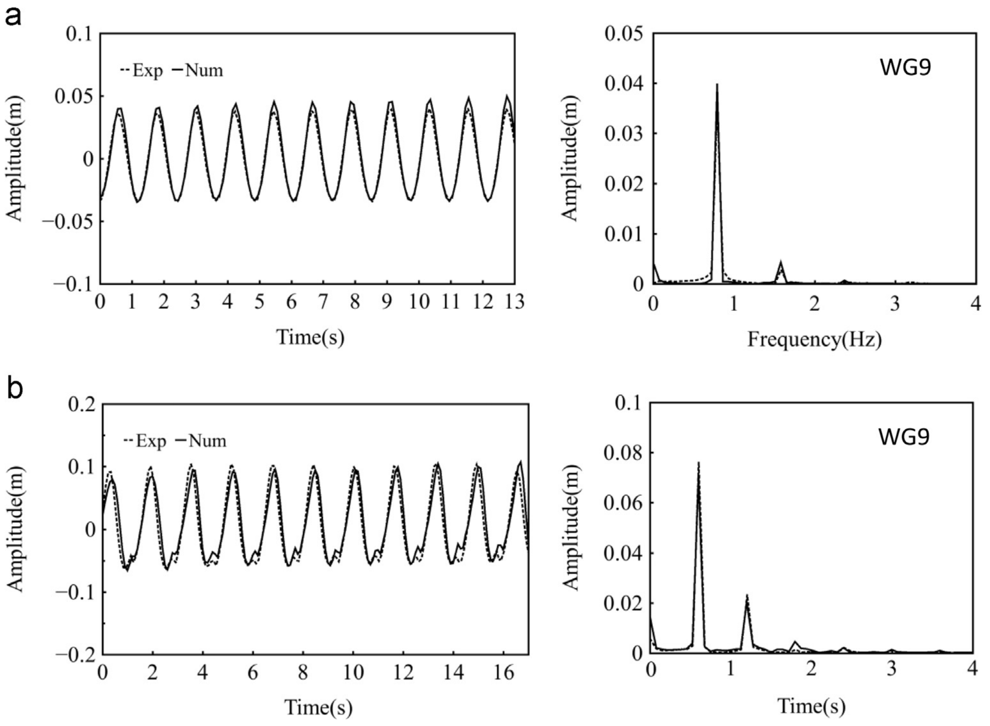

Fig. 10. Time series of free surface elevation and amplitude spectra for regular wave cases R1 and R3. (a) Case R1 and (b) case R3.

for the cases R1, R2 and R3 are about 21%, 31% and 40% of its linear horizontal wave loading, respectively. Additionally, the fourth order horizontal wave loading can be clearly seen for cases R2 and R3.

3.4.2. Focused wave groups

3.4.2.1. Free surface elevations. Both numerical and experimental results for the free surface elevations at six selected locations for the case F3 are shown in Fig. 12, as well as the corresponding amplitude spectra. As with regular waves, a careful match between experiments and numerical models for WG1 was made to ensure that the incoming waves in the numerical tank are close to the experiments. Note that WG19 is placed close to the side wall of the numerical wave tank for a second check of the incoming waves, though in the experiments, it is 3 m off the central line. WG5 is about 1 m in front of the cylinder, where a focused wave group becomes more compact. WG9 is the focused point, where all wave components come into phase and a large energetic event is produced. At location WG13, which is 2 mm behind the downstream stagnation point of the cylinder, wave breaking was observed in some of the test cases. This may lead to a relatively

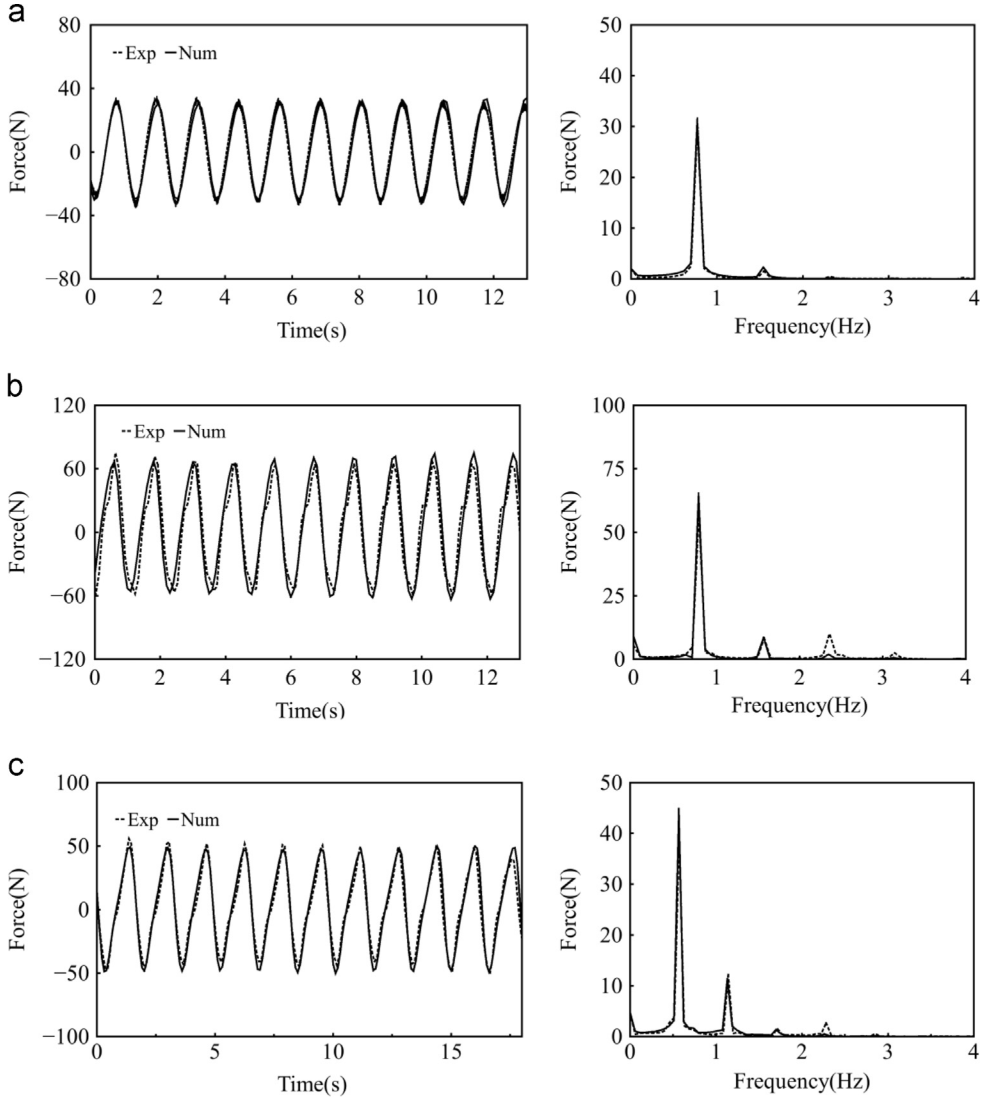

Fig. 11. Time series of horizontal forces on the cylinder and amplitude spectra for all the three regular wave cases. (a) Case R1, (b) case R2 and (c) case R3.

larger discrepancy between the predicted and measured values of the free surface elevations due to the symmetry used in the computational model. The focused wave group becomes less compact due to frequency dispersion at location WG17, which is about 1 m behind the cylinder. Apart from WG13, the numerical model appears to have captured all the main physical features of the nonlinear focused wave interaction with the vertical cylinder, with close matching of both crest values of the free surface and the wave shapes. Additionally, from the amplitude spectra, it can be seen that the present model correctly represents the frequency of all major harmonics which are present, and accurately predicts the amplitude of these harmonics. The average difference between the crests obtained by the numerical model and the experiments is about 6% and the maximum difference is about 15%.

In this paper, free surface elevations at WG9 for cases F2, F3 and F4 are presented in Fig. 13. Similar to regular waves, for all the focused wave cases presented in this paper, OpenFOAM has performed very well and has correctly captured all the wave harmonics and the crest values. Comparisons among these four cases demonstrate that steeper focused wave groups (F2 and F4) produce stronger nonlinear wave–structure interactions with larger 2nd order waves and also the 3rd order waves. From the cases F1 to F4, the contributions of nonlinear free surface run-up are 20%, 35%, 30% and 43% of its linear free surface elevation.

Fig. 14 shows several snapshots of the wave field around the cylinder for the case F4. The maximum wave run-up occurs when peak wave crest hit on the cylinder. The scattered waves around the cylinder shown in Fig. 14 is very close to those captured by Sheikh and Swan (2005) during their experiments, in which wave steepness and cylinder slenderness are in the similar range with the test case F4 used in our study. The Type 1 and Type 2 of scattered wave as specified by Sheikh and Swan (2005) can be clearly seen in the three dimensional wave field produced by our numerical simulation, labelled in Fig. 13as well. The run-up and subsequent wash-down of fluid on the front face of the cylinder will form the scattered waves of Type 1 while Type 2 originates from an oscillation of fluid around the surface of the cylinder. The details can be found in the aforementioned reference.

3.4.2.2. Horizontal wave loading. The comparisons of horizontal wave loading time histories on the cylinder between the modelled results and the experimental measurements are shown in Fig. 15. Similar to the free surface elevations, the horizontal forces obtained by the present model match the experimental data well. Having achieved good agreements for all the cases discussed in this paper for both regular waves and focused wave groups, we are confident that OpenFOAM is capable of modelling nonlinear

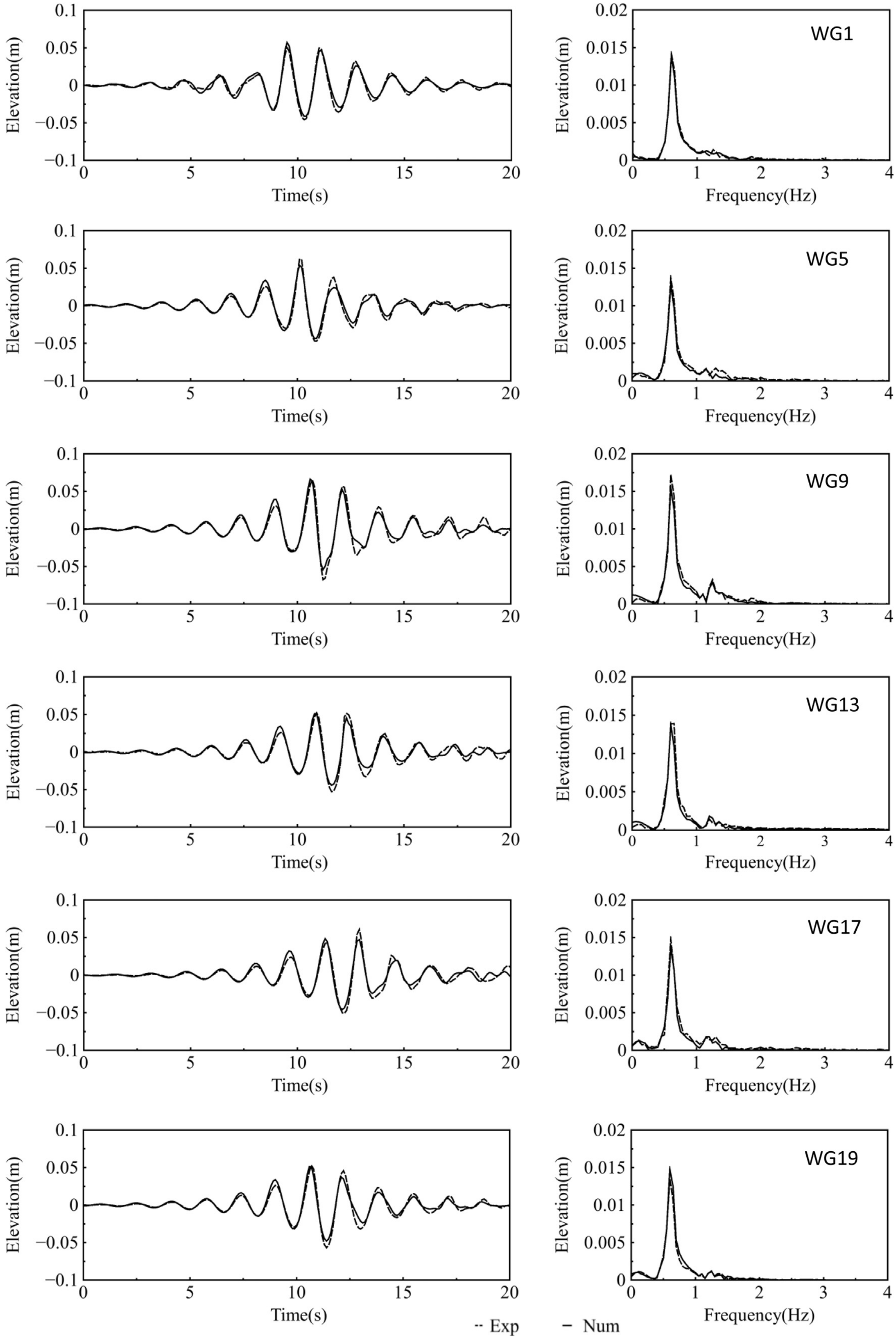

Fig. 12. Time series of free surface elevation and amplitude spectra for focused wave group case F3.

wave interactions with structures accurately, including both free surface run-up and wave loading. Compared with free surface run-up, the nonlinear effect for wave loading is less significant. This has presented the same phenomenon that was observed from the numerical simulation using 2nd order potential flow theory (Zang et al., 2003). In the 2nd order diffraction calculation, it has been

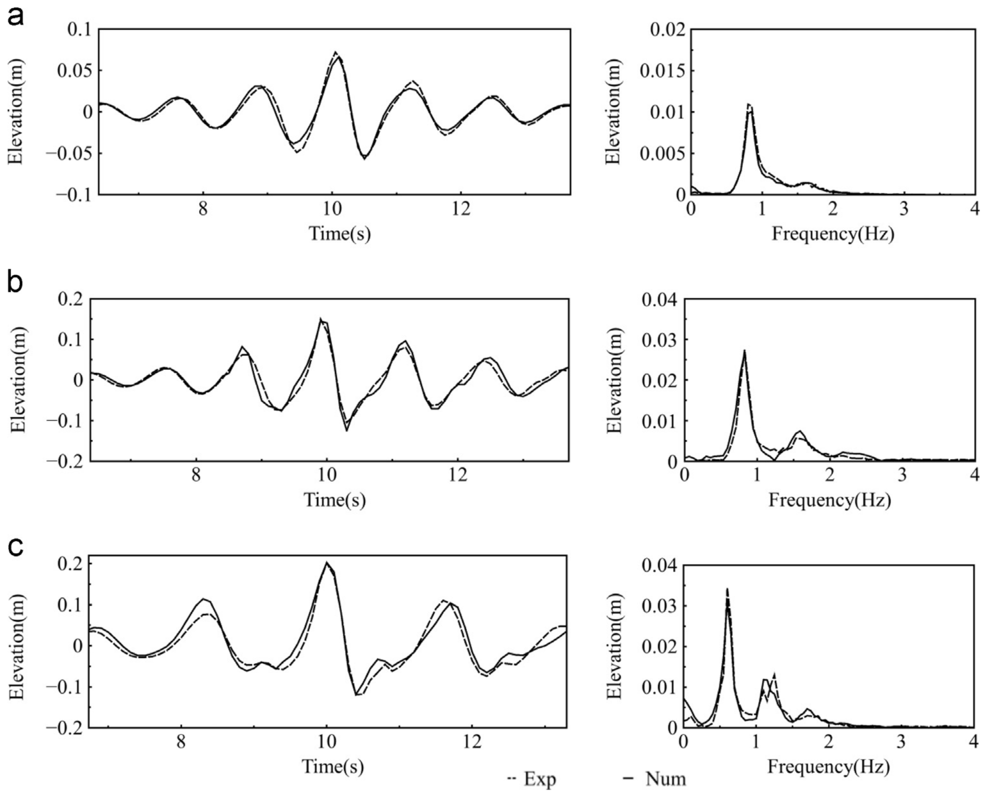

Fig. 13. Time series of free surface elevation and amplitude spectra at WG9 for focused wave group cases. (a) Case F1, (b) case F2 and (c) case F4.

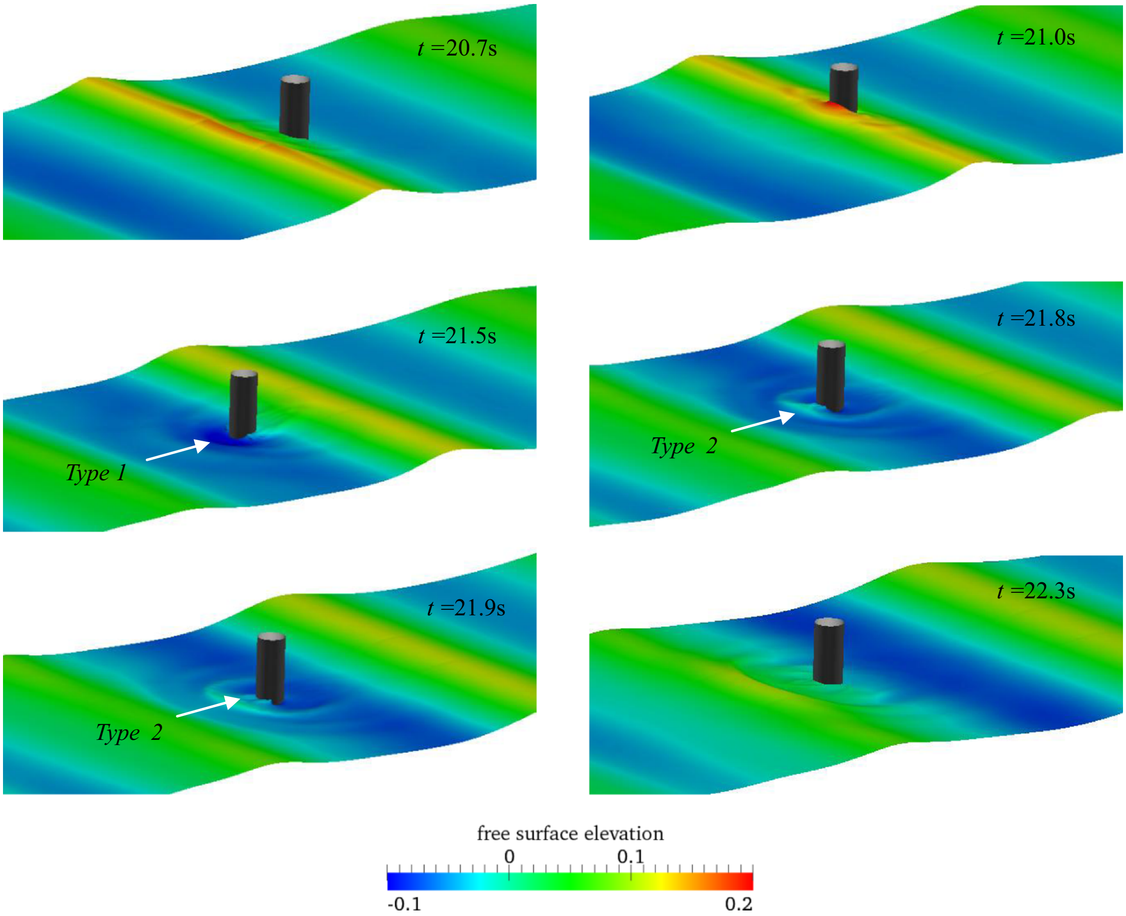

Fig. 14. 3D views of the focused wave group impacting on the cylinder at several moments. The free surface level is shaded from blue to red. And the unit for the color legend is m.

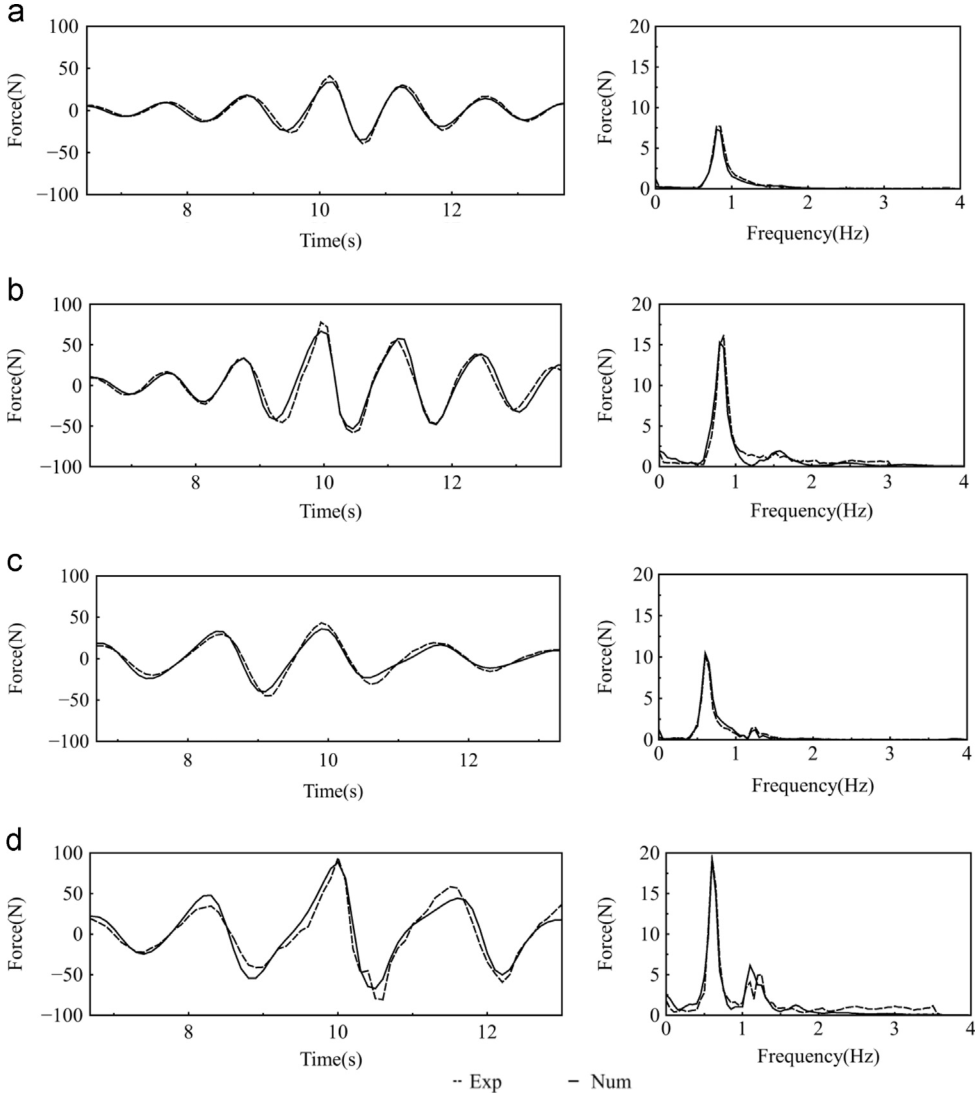

Fig. 15. Time series of horizontal wave loading on the cylinder and amplitude spectra for the four focused wave group cases. (a) Case F1, (b) case F2, (c) case F3 and (d) case F4.

found that the 2nd order loading due to the product of linear term is 180° degree phase shift from the 2nd order loading due to 2nd order potential.

3.4.2.3. Spectral decomposition. It is generally known that the nonlinear effects are important in offshore engineering, particularly for large waves. The higher order harmonics may be significant enough to cause “ringing”, which is resonance of the structure induced by wave–structure interaction (Swan et al., 1997). In order to extract the harmonic structure of wave loading and free surface run-up on the cylinder, both crest focused waves (C, say) and trough focused waves (T, say), obtained by multiplying the signal by -1, were generated, both in the experiments and in the numerical simulations. Following Fitzgerald et al. (2012) and Zang et al. (2006, 2010a, 2010b), a simple phase-based separation method has been applied. Assuming the existence of a Stokes-like harmonic series in both wave steepness and frequency, the odd and even harmonics can be obtained by doing subtraction, $(C-T)/2$, and addition, $(C+T)/2$, respectively. $(C-T)/2$ only contains linear harmonics, 3rd order, 5th order etc., while $(C+T)/2$ contains 2nd order difference, 2nd order sum, 4th order…. The focused wave group can then be separated into its fundamental components by digital filtering. Focused wave groups are compact and have continuous wave spectra. There is considerable overlap between adjacent harmonics, so the alignment of the signals between the crest focused waves and trough focused waves should be checked carefully to minimise the “leakage” between the crest and trough signals by taking the minimum of cross correlation between signals (Mclaughlan, 2011).

The harmonic structures of free surface elevation at WG9 for case F4 were obtained by combining the free surface time histories of crest-focused wave group with that of a trough-focused wave group. This was done for both experiments and numerical simulations, and results are compared in Fig. 16. From top to bottom are long wave, linear, 2nd, 3rd and 4th harmonics. Apart from the linear free surface elevation, the long wave, 2nd, 3rd and 4th order harmonics also have good agreement with the experiments, with close matching of both crest values and the wave shapes.

Similar results have been obtained for the case F3, shown in Fig. 17. It is clear that the numerical predictions match the experimental results very well up to 3rd order harmonics for this case. Even for the 4th order harmonics, which is less than 7% of its linear component, the present model can represent the wave shape correctly, shown in Fig. 18. The harmonic structures of horizontal forces on the cylinder are shown in Figs. 19 and 21 for the cases F4 and F3. Then the comparisons of the wave shapes of the 4th order horizontal forces for the cases F4 and F3 are shown

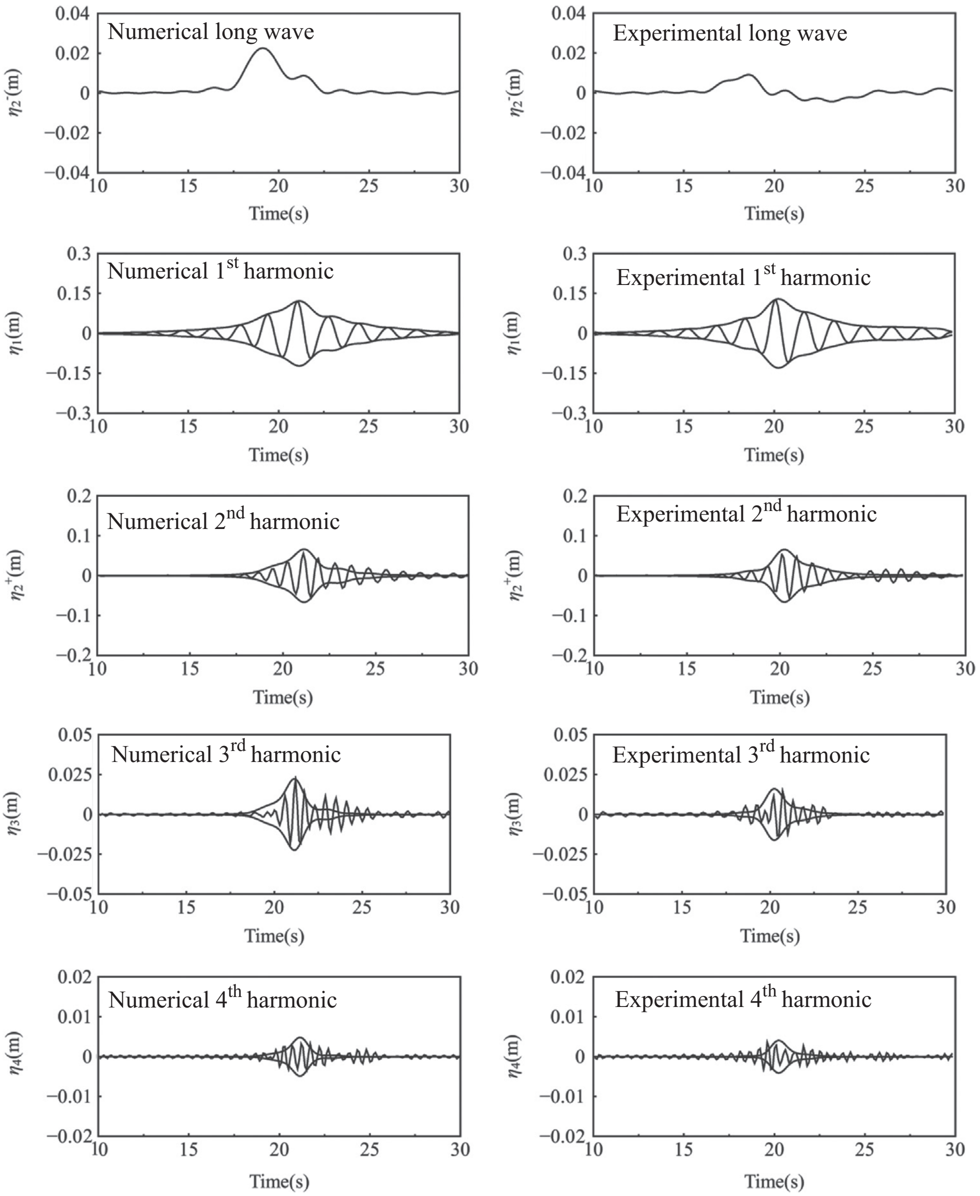

Fig. 16. The harmonic structures of free surface elevation for focused wave group case F4.

in Fig. 20 and Fig. 22, respectively. The direct comparisons between cases F3 and F4 can be seen in Fig. 23.

The harmonics of both free surface and horizontal loading for both cases are enveloped to display how the wave energy is distributed. Noting that the applied separation method is based on the assumption that there is a generalised Stoke-type expansion for a wave group, therefore, the envelope of each harmonic above 2nd order can be derived from the envelope of the linear component. Wave envelopes for each harmonic component for case F4 and case F3 are shown in Figs. 16, 17, 19 and 21 as well. From top to bottom are long wave, linear, 2nd, 3rd and 4th harmonics. The envelope of linear component is obtained by applying the Hilbert Transform as usual (Mclaughlan, 2011). The *n*th harmonic envelope is obtained by raising the fundamental envelope to the power *n* and its height is scaled by applying least square method to match the size of the maximum of the measured *n*th order harmonic. There is a good agreement between the approximated envelops and the harmonic wiggles up to the 4th harmonics for case F3 and case F4, showing that the harmonic shapes can be reconstructed from the knowledge of the linear component alone and a Stokes-type scaling for the force and the wave run-up might be possible. Apart from 2nd and 3rd harmonics, the applied method works well for all terms up to 4th harmonic. The second pulse of waves in the second harmonic component arises because only a linear stoke wave is used as the input signal in the numerical simulations, but the waves which are created are inherently nonlinear. There are several possible reasons for the slight mismatch of 3rd order harmonics, for example, nonlinear free-surface forces in potential flow, fluid dynamic drag and the secondary load cycle observed on the cylinder in steep waves (Zang et al., 2010).

Now, the idea of the amplitude scaling is examined by comparing small and large wave groups with approximately the same peak frequency, shown in Fig. 23. It can be seen from the figures that the Stokes scaling applies in these cases. The scaling coefficients, which are the ratio of the peak heights of the linear wave envelopes for the large and small wave groups at the position of the front stagnation point of the cylinder in the absence of the cylinder, is 2.0 for cases F3 and F4. Stokes scaling allows us to find the *n*th force harmonic of scaled amplitude wave groups of

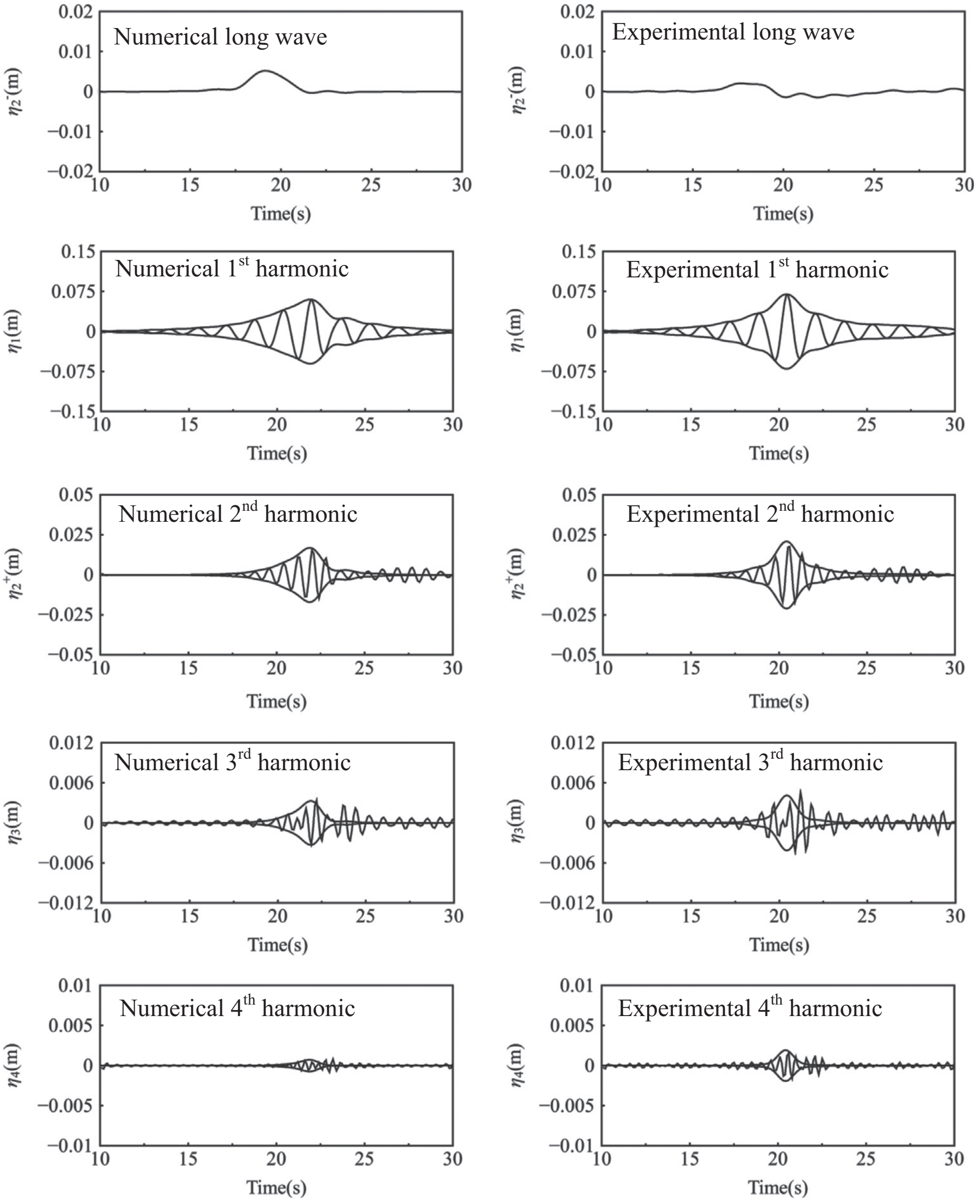

Fig. 17. The harmonic structures of free surface elevation for focused wave group case F3.

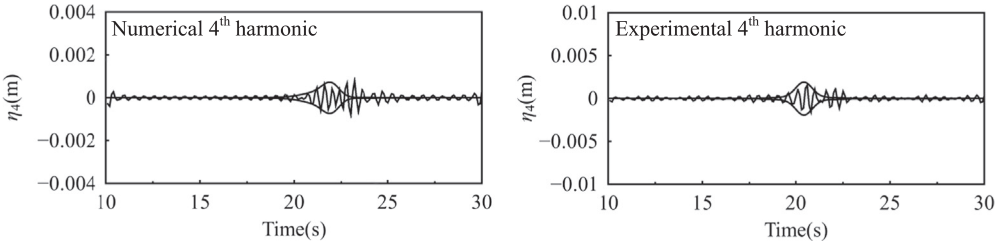

Fig. 18. Time histories of 4th order free surface elevation for focused wave group case F3.

the same frequency by multiplying the scaling coefficient raised to the power n.

Additionally, it can be seen from Fig. 23 that for a larger wave (case F4), the 2nd order harmonic is about 40% of its linear component and for the small wave (case F3), the contribution of 2nd order harmonic is about 20% of the first order harmonic force. It is clear that the higher order nonlinear effects should not be neglected otherwise a considerable percentage of energy would be missed.

4. Conclusions

OpenFOAM has been used in the present study to model nonlinear wave interactions with a vertical cylinder. The new modules developed to advance the wave generation and absorbing capacities of the numerical model are proved to work well for all the test cases discussed in this paper. The specified waves, including regular waves and focused wave groups, have been generated in the numerical wave tank by providing necessary

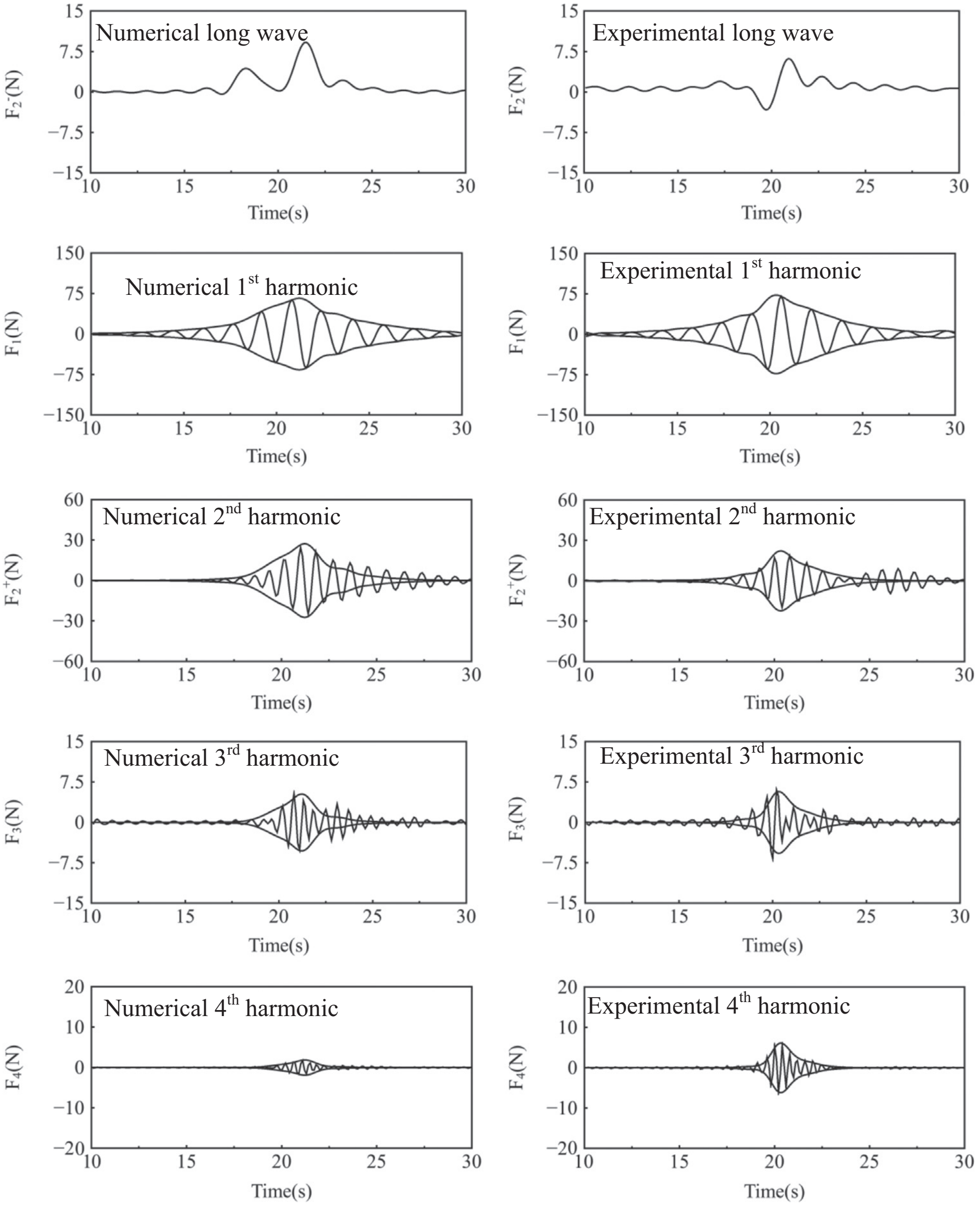

Fig. 19. The harmonic structures of horizontal forces for case F4.

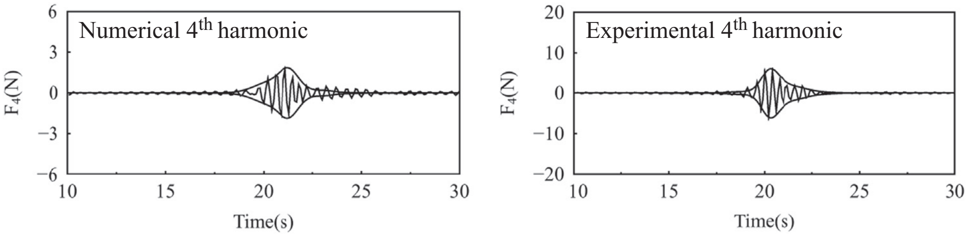

Fig. 20. Time histories of 4th order horizontal forces for focused wave group case F4.

wave parameters. With the added relaxation zone at the end of the numerical wave tank, waves dissipate gradually inside the relaxation zone minimizing wave reflections. Thus the computational cost has been reduced significantly by applying the relaxation technique compared to using the wave tank without the damping zone. Linking the default solver, *interFoam*, with the functions specified in the new module, the non-linear wave interaction with a vertical cylinder up to at least 4th order harmonic have been predicted accurately. Extra attention should be paid to mesh refinement and density to obtain convergent results. Generally, the resolution of $L/70$ in the horizontal direction and $H/8$ in the vertical direction would be adequate. There may be benefits to using third party mesh generation tools such as Salome and Gmsh (Kortelainen, 2009).

By using the crest-trough phase-based separation method, we can reproduce harmonic structure in the wave loading on the structure and free surface elevations. The harmonic shapes can be reconstructed from the knowledge of the linear component alone

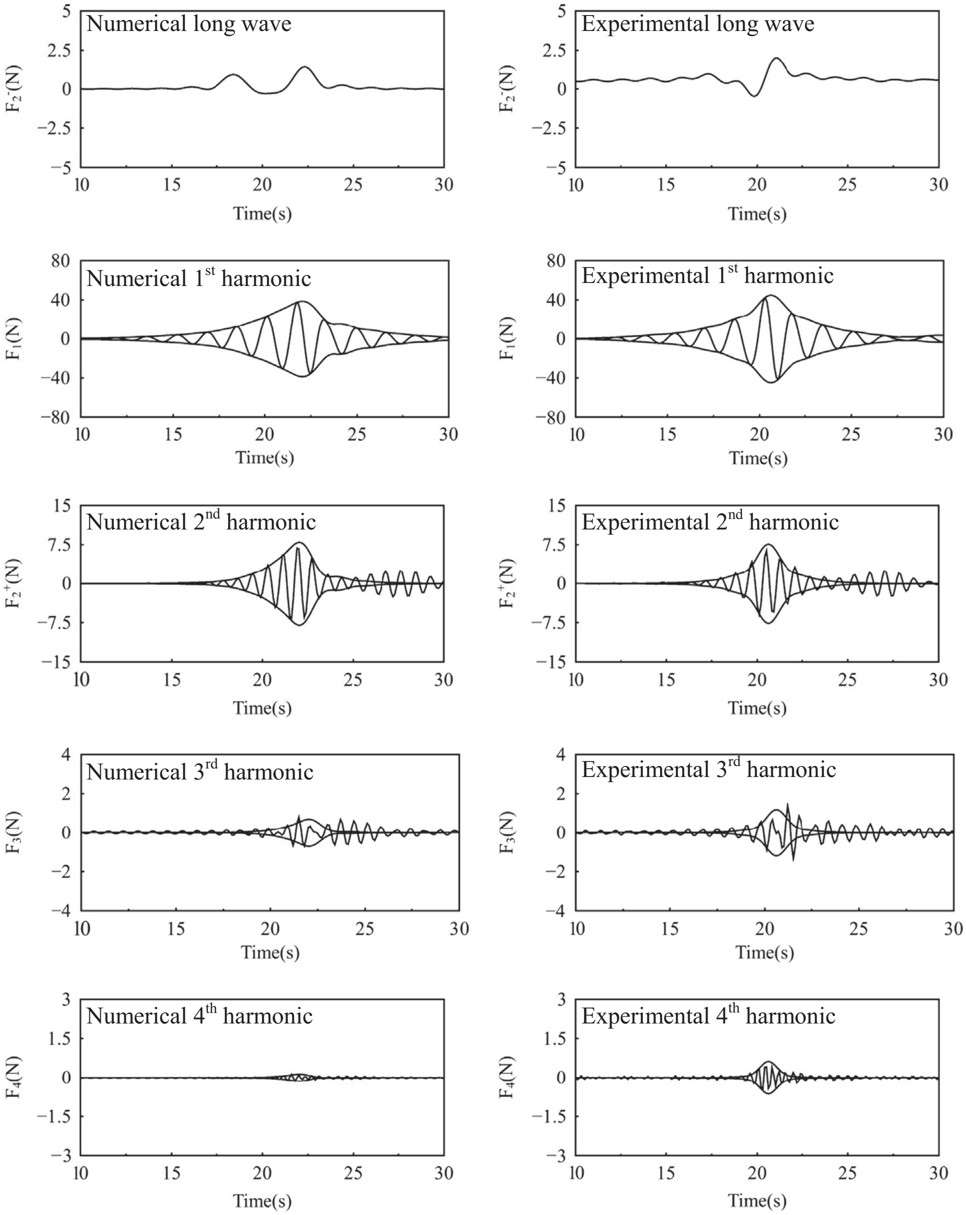

Fig. 21. The harmonic structures of horizontal forces for focused wave group case F3.

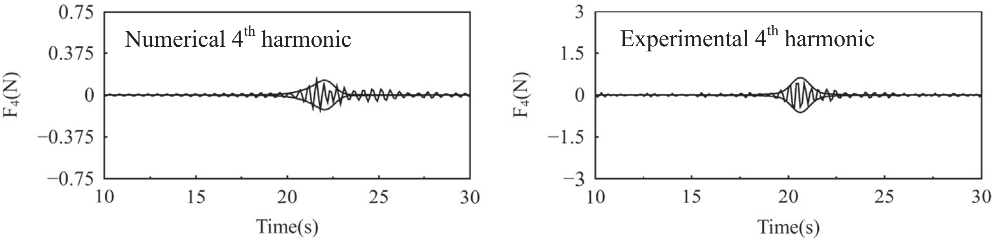

Fig. 22. Time histories of 4th order horizontal forces for focused wave group case F3.

by raising the fundamental envelope to the power n and the nth force harmonic of scaled amplitude wave groups of the same frequency can be found by multiplying the scaling coefficient raised to the power n. Additionally, it is clear that using linear theory would not be adequate and leads to inaccuracy with up to 50% of the total wave loading loss.

Comparisons between the numerical results and the measured data for three regular waves and four focused wave groups, have indicated that OpenFOAM is very capable of accurate modelling of nonlinear wave interaction with offshore structure, with up to 4th order harmonics correctly captured. This has shown the great potential of OpenFOAM for the further applications to the violent

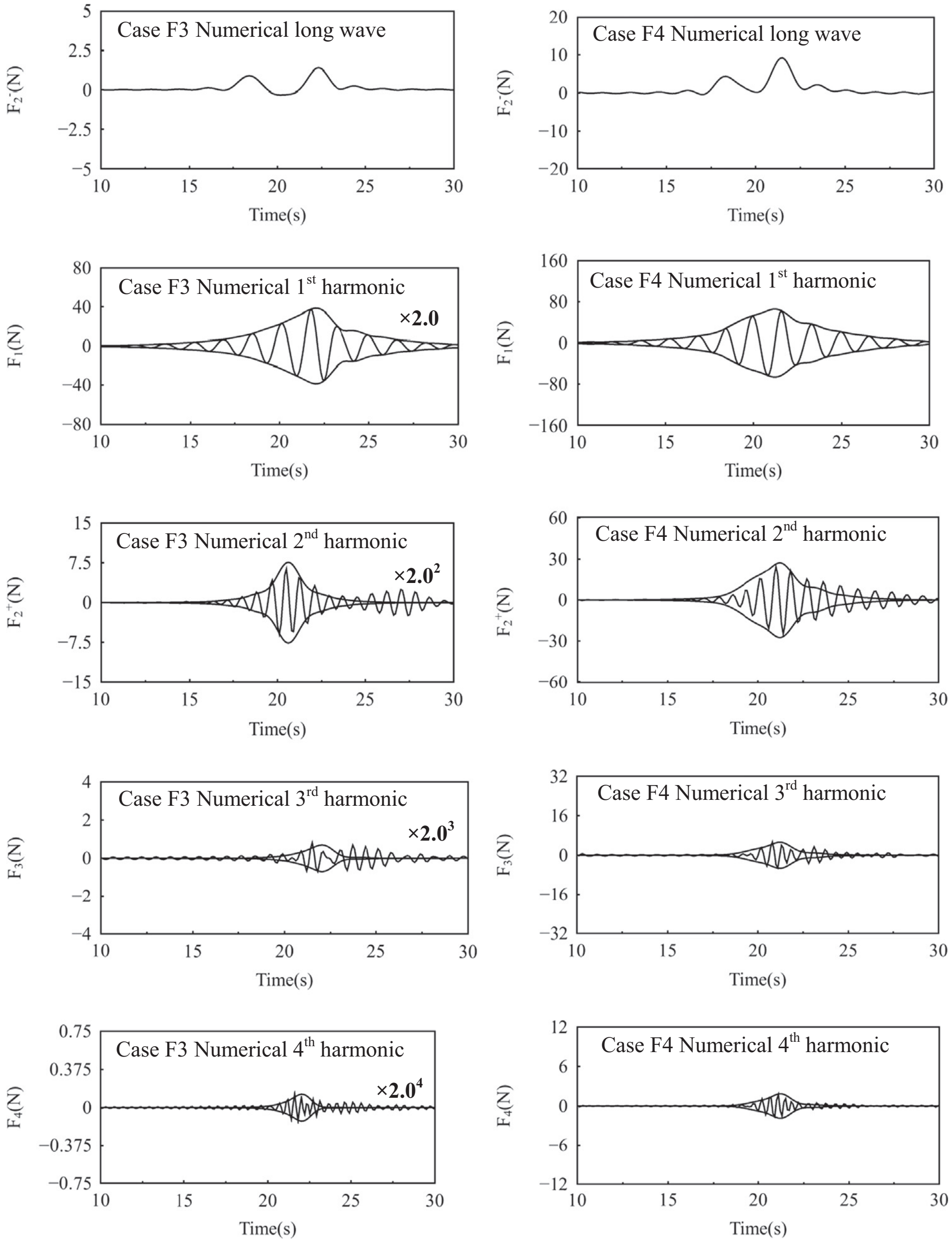

Fig. 23. The harmonic structures of horizontal wave loading on the cylinder and the envelops for both focused wave group cases F3 and case F4. From top to bottom: long wave, linear, 2nd, 3rd and 4th harmonic.

wave impact on offshore wind turbine foundations, wave energy devices and floating structures. The 6 DoF motions of floating structures can be determined by solving the equation of motions for rigid bodies and then the whole mesh can be updated by using the built-in mesh motion solver supplied with OpenFOAM.

Acknowledgements

We are very grateful for the reviewers' constructive comments and suggestions, which have helped us to improve the quality of this paper. The first author acknowledges the financial support of the University of Bath (Grant no: 3451 and 3708) and China Scholarship Council (CSC) (Grant no: 2011606036) for her PhD study. We thank Jens Kirkegaard and all the staff at DHI for their help and hospitality during the experiments, which have been supported by European Community's Sixth Framework Programme through the grant to the budget of the Integrated Infrastructure Initiative HYDRALAB III within the Transnational Access Activities, Contract no. 022441. We also thank Prof. Paul Taylor, Jana Orszaghova, James Grice from Oxford, Robert Stringer from Bath and Menases Tello from Lisbon, for their involvement in the experiments. We are also grateful for the use of the HPC facility at University of Bath for some of the numerical analysis.

References

Bai, W., Eatock Taylor, R., 2007. Numerical simulation of fully nonlinear regular and focused wave diffraction around a vertical cylinder using domain decomposition. Appl. Ocean Res. 29, 55–71.

Celebi, M.S., Kim, M.H., Beck, R.F., 1998. Fully nonlinear 3-D numerical wave tank simulation. J. Ship Res. 42 (1), 33–45.

Chau, F.P., Eatock Taylor, R., 1992. Second-order wave diffraction by a vertical cylinder. J. Fluid Mech. 240, 571–599.

Courant, R., Friedrichs, K., Lewy, H., 1967. On the partial difference equations of mathematical physics. IBM J. Res.Dev. 11 (2), 215–234.

Datta, B.N., 2010. Numerical Linear Algebra and Applications, second ed. SIAM, Philadelphia.

Ferziger, J., Peric, M., 1999. Computational Methods for Fluid Dynamics, second ed. Springer, Berlin.

Fitzgerald, C., Grice, J., Taylor, P.H., Eatock Taylor, R., Zang, J., 2012. Phase manipulation and the harmonic components of ringing forces on a surface-piercing column. In: 27th IWWWFB. Copenhagen, Denmark.

Folley, M., Whittaker, T., Osterried, M., 2004. The oscillating wave surge converter. In: 14th International Offshore and Polar Engineering Conference. Toulon, France.

Goda, Y., Suzuki, Y., 1976. Estimation of incident and reflected waves in random wave experiements. In: Proceedings of the 15th International Conference on Coastal Engineering, ASCE. 1:828–845.

Grilli, S.T., Guyenne, P., Dias, F., 2001a. A fully nonlinear model for three-dimensional overturning waves over arbitrary bottom. Int. J. Numer. Methods Fluids 35 (7), 829–867.

Grilli, S.T., Guyenne, P., Dias, F., 2001b. Three-dimensional numerical model for fully nonlinear waves over arbitrary bottom. In: WAVES 2001 Conf. San Francisco, USA.

Hasselmann, K., Barnett, T.P., Bouws, E., 1973. Measurements of wind-wave growth and swell decay during the Joint North Sea Wave Project (JONSWAP). Dtsch. Hydrogr. Z A8 (Suppl. 12), 1–95.

Higuera, P., Lara, J.L., Losada, I.J., 2013a. Realistic wave generation and active wave absorption for Navier–Stokes models application to OpenFOAM®. Coastal Eng. 71, 102–118.

Higuera, P., Lara, J.L., Losada, I.J., 2013b. Simulation coastal engineering processes with OpenFOAM®. Costal Eng. 71, 119–134.

Hirt, C.W., Nichols, B.D., 1981. Volume of fluid (VOF) method for the dynamics of free boundaries. J. Comput. Phys. 39, 201–225.

Issa, R.I., 1985. Solution of the implicitly discretised fluid flow equations by operator-splitting. J. Comput. Phys. 62, 40–65.

Jacobsen, N.G., Fuhrman, D.R., Fredsøe, J., 2012. A wave generation toolbox for the open-source CFD library: OpenFoam®. Int. J. Numer. Methods Fluids 70, 1073–1088.

Keulegan, H., Carpenter, H., 1958. Forces on cylinders and plates in an oscillating fluid. J. Res. Nat. Bur. Stand. 60, 423–440.

Kim, M.H., Yue, D.K.P., 1989. The complete second-order diffraction solution for an axisymmetric body Part 1. Monochromatic incident waves. J. Fluid Mech. 200, 235–264.

Kim, M.H., Yue, D.K.P., 1990. The complete second-order diffraction solution for an axisymmetric body Part 2. Bichromatic incident waves and body motions. J. Fluid Mech. 211, 557–593.

Kortelainen, J., 2009. Meshing Tools for Open Source CFD—A Practical Point of View. Research Report, No. VTT-R-02440-09. VTT, Espoo, Finland.

LeVeque, R., 2002. Finite Volume Methods for Hyperbolic Problems. Cambridge University Press.

Larsen, J., Dancy, H., 1983. Open boundaries in short wave simulations—a new approach. Coastal Eng. 7, 285–297.

Ma, Q.W., Wu, G.X., Eatock Taylor, R., 2001a. Finite element simulation of fully non-linear interaction between vertical cylinders and steep waves. Part 1: Methodology and numerical procedure. Int. J. Numer. Methods Fluids 36, 265–285.

Ma, Q.W., Wu, G.X., Eatock Taylor, R., 2001b. Finite element simulations of fully non-linear interaction between vertical cylinders and steep waves. Part 2: numerical results and validation. Int. J. Numer. Methods Fluids 36, 287–308.

Mclaughlan, S., 2011. Wave Loading on Offshore Wind Turbine Columns. Final Year Project Report, Department of Engineering Science. University of Oxford, Oxford.

Mendez, F.J., Losada, I.J., Losada, M.,A., 2001. Wave—induced mean magnitudes in permeable submerged breakwaters. J. Waterw. Port Coastal Ocean Eng. 127, 7–15.

Morgan, G., Zang, J., Greaves, D., Heath, A., Whitlow, C., Young, J., 2010. Using the rasInterFoam CFD model for wave transformation and coastal modelling. In: Proceedings of 32nd Conference on Coastal Engineering. Shanghai, China, 2010.

Morgan, G., Zang, J., 2011. Application of OpenFOAM to coastal and offshore modelling. In: The 26th IWWWFB. Athens, Greece.

Morison, J.R., O'Brien, M.P., Johnson, J.W., Schaaf, S.A., 1950. The force exerted by surface waves on piles. J. Petrol. Technol. 2 (5), 149–154.

Romate, J.E., 1992. Absorbing boundary conditions for free surface waves. J. Comput. Phys. 99, 135–145.

Sarpkaya, T., Isaacson, M., 1981. Mechanics of Wave Forces on Offshore Structures. Van Nostrand Reinhold, New York, NY.

Sheikh, R., Swan, C., 2005. The interaction between steep waves and a vertical, surface-piercing column. J. Offshore Mech. Arct. Eng 127, 31–38.

Stansberg, C.T., Kristiansen, T., 2005. Non-linear scattering of steep surface waves around vertical columns. Appl. Ocean Res. 27 (2), 65–80.

Swan, P., Taylor, P.H., Van Langer, H., 1997. Observations of wave–structure interaction for a multi-legged concrete platform. Appl. Ocean Res. 19, 309–327.

Taylor, P.H., Williams, B.A., 2004. Wave statistics for intermediate water depth—new waves and symmetry. J. Offshore Mech. Arct. Eng. 126, 54–59.

The OpenFOAM® Foundation, 2011a. The Open Source CFD Toolbox of OpenFOAM: Programmer's Guide.

The OpenFOAM® Foundation, 2011b. The Open Source CFD Toolbox of OpenFOAM: User Guide.

Weller, H.G., Tabor, G., Jasak, H., Fureby, C., 1998. A tensorial approach to computational continuum mechanics using object oriented techniques. Comput. Phys. 12 (6), 620–631.

Walker, D.A.G., Eatock Taylor, R., Taylor, P., Zang, J., 2008. Wave diffraction and near-trapping by a multi-column gravity based structure. Ocean Eng. 35 (2), 201–229.

Walker, D.A.G., Taylor, P.H., Eatock Taylor, R., Zang, J., Tromans, P.S., 2007. Water wave diffraction and the spectral response surface method. Int. J. Offshore Polar Eng. 17 (4), 254–258.

Zang, J., Gibson, R., Taylor, P.H., Eatock Taylor, R., Swan, C., 2006. Second order wave diffraction around a fixed ship-shaped body in unidirectional steep waves. J. Offshore Mech. Arct. Eng. 128 (2), 89–99.

Zang, J., Liu, S., Eatock Taylor, R., Taylor, P.H., 2009. Wave run-up and response spectrum for wave scattering from a cylinder. Int. J. Offshore Polar Eng. 19 (3), 183–188.

Zang, J., Taylor, P.H., Eatock Taylor, R., 2003. Hydrodynamics of Ship-shaped Floating Bodies. REBASDO Progress Report, Department of Engineering Science. University of Oxford.

Zang, J., Taylor, P.H., Morgan, G., Tello, M., Grice, J., Orszaghova, J., 2010. Experimental study of non-linear wave impact on offshore wind turbine foundations. In: Proceedings Third International Conference on the Application of Physical Modelling to Port and Coastal Protection. Barcelona, Spain.

Zang, J., Taylor, P.H., Morgan, G., Stringer, R., Orszaghova, J., Grice, J., Tello, M., 2010. Steep wave and breaking wave impact on offshore wind turbine foundations—ring re-visited. In: The 25th IWWWFB. Harbin, China.